

# Barium & related stars and their white-dwarf companions <sup>★</sup>

## I. Giant stars

A. Jorissen<sup>1</sup>, H.M.J. Boffin<sup>2</sup>, D. Karinkuzhi<sup>1,3</sup>, S. Van Eck<sup>1</sup>, A. Escorza<sup>1,4</sup>, S. Shetye<sup>1,4</sup>, and H. Van Winckel<sup>4</sup>

<sup>1</sup> Institut d'Astronomie et d'Astrophysique, Université Libre de Bruxelles, Campus Plaine C.P. 226, Boulevard du Triomphe, B-1050 Bruxelles, Belgium e-mail: ajorisse, svaneck@ulb.ac.be

<sup>2</sup> ESO, K. Schwarzschild Straße 2, Garching bei München, Germany  
e-mail: hboffin@eso.org

<sup>3</sup> Department of Physics, Bangalore University, Jnana Bharathi Campus, Bangalore, India 560056

<sup>4</sup> Institute of Astronomy, KU Leuven, Celestijnenlaan 200D, 3001 Leuven, Belgium

Received X; accepted Y

### ABSTRACT

**Context.** Barium and S stars without technetium are red giants suspected of being all members of binary systems.

**Aims.** This paper provides both long-term and revised, more accurate orbits for barium and S stars adding to previously published ones. The sample of barium stars with strong anomalies comprise all such stars present in the Lü et al. catalogue.

**Methods.** Orbital elements are derived from radial velocities collected from a long-term radial-velocity monitoring performed with the HERMES spectrograph mounted on the Mercator 1.2 m telescope. These new measurements were combined with older, CORAVEL measurements. With the aim of investigating possible correlations between orbital properties and abundances, we collected as well an as homogeneous as possible set of abundances for barium stars with orbital elements.

**Results.** We find orbital motion for all barium and extrinsic S stars monitored. We obtain the longest period known so far for a spectroscopic binary involving an S star, namely 57 Peg with a period of the order of 100 – 500 yr. We present the mass distribution for the barium stars, which ranges from 1 to 3  $M_{\odot}$ , with a tail extending up to 5  $M_{\odot}$  in the case of mild barium stars. This high-mass tail comprises mostly high-metallicity objects ( $[Fe/H] \geq -0.1$ ). Mass functions are compatible with WD companions whose masses range from 0.5 to 1  $M_{\odot}$ . Strong barium stars have a tendency to be found in systems with shorter periods than mild barium stars, although this correlation is rather loose, metallicity and WD mass playing a role as well. Using the initial – final mass relationship established for field WDs, we derived the distribution of the mass ratio  $q' = M_{AGB,ini}/M_{Ba}$  (where  $M_{AGB,ini}$  is the WD progenitor initial mass, i.e., the mass of the system former primary component) which is a proxy for the initial mass ratio (the more so, the less mass the barium star has accreted). It appears that the distribution of  $q'$  is highly non uniform, and significantly different for mild and strong barium stars, the latter being characterized by values mostly in excess of 1.4, whereas mild barium stars occupy the range 1 – 1.4.

**Conclusions.** The orbital properties presented in this paper pave the way for a comparison with binary-evolution models.

**Key words.** binaries: spectroscopic – white dwarfs – stars: late-type – stars: peculiar (except chemically peculiar) – stars: AGB and post-AGB – stars: abundances

## 1. Introduction

Barium stars (Bidelman & Keenan, 1951) are a class of G-K red-giant stars with strong spectral lines of barium and other elements produced by the s-process of nucleosynthesis (Käppeler et al., 2011). Similar spectral peculiarities are found as well in main-sequence stars, known as barium dwarfs, which cover spectral types all the way from F to K (North et al., 1994). Another related family comprises S stars (Keenan, 1954), which are giants cooler than barium stars, exhibiting ZrO bands in their spectra. As shown by e.g. Smith & Lambert (1988) and Jorissen et al. (1993), S stars arise in two flavours: Tc-rich (also known as intrinsic) and no-Tc (also known as extrinsic) S stars, depending on the presence or absence of Tc lines, an element with no stable isotopes. Extrinsic S stars are the cooler analogues of barium stars.

These families of stars exhibiting strong lines of s-process elements have been intensively studied in the past (e.g., Burbidge & Burbidge, 1957; Warner, 1965; McClure et al., 1980; Boffin & Jorissen, 1988; McClure & Woodsworth, 1990; Jorissen & Mayor, 1992; North et al., 1994; Jorissen et al., 1998; North et al., 2000; de Castro et al., 2016; Merle et al., 2016), being benchmarks of post mass-transfer binaries involving low- and intermediate-mass stars. They provide strong constraints on the mass-transfer phase they experienced when the former primary, now a white dwarf, was an asymptotic giant branch (AGB) star and transferred material enriched in heavy elements produced by the s-process of nucleosynthesis (e.g., Käppeler et al., 2011), among which barium. The polluted companion indeed kept this chemical signature up to now, long after the mass transfer ceased, and exhibits strong absorption lines of ionised barium in its spectrum. This binary scenario was convincingly confirmed by the observation that statistically all barium stars reside in binary systems (McClure et al., 1980; McClure, 1983; Jorissen & Mayor, 1988; McClure & Woodsworth, 1990; Jorissen et al., 1998).

<sup>★</sup> Based on observations made with the Mercator Telescope, operated on the island of La Palma by the Flemish Community, at the Spanish Observatorio del Roque de los Muchachos of the Instituto de Astrofísica de Canarias.

Previous binary-evolution models have shown how difficult it is to account for the orbital properties of these objects (Pols et al., 2003; Jorissen, 2003; Bonačić Marinović et al., 2008). These models need improved prescriptions for the mass-transfer process (Frankowski & Jorissen, 2007; Izzard et al., 2010; Dermine et al., 2011). These studies have shown how important it is to derive the orbital periods and eccentricities of post-mass transfer systems such as barium stars, to constrain evolutionary models. CH and Carbon-Enriched Metal-Poor (CEMP) stars are post-mass-transfer objects as well, albeit of low metallicity, and new and updated orbits for these classes were presented in a recent paper (Jorissen et al., 2016). Post-AGB stars with a near-infrared excess indicative of a dusty disc form another, possibly related, family of post-mass-transfer objects (e.g., Van Winckel et al., 2009; Oomen et al., 2018).

Orbital elements provide constraints on evolutionary models through the period – eccentricity ( $P - e$ ) diagram and the mass-function distribution, which is sensitive to the companion's mass. For post-mass-transfer systems (like barium, CH and CEMP-s systems enriched in heavy elements synthesised by the s-process), the companion should be a CO white dwarf (Merle et al., 2016). This paper presents the orbits for all known giant barium stars with strong chemical anomalies (i.e., all those classified as Ba3, Ba4, or Ba5 in the 1983 edition of the Lü et al. catalogue), plus an extended sample of mild barium stars, along with their cooler analogues, the extrinsic S stars lacking the unstable element technetium. A detailed analysis of the mass functions, the mass-ratio and mass distributions, the  $P - e$  diagram, and their relationship with chemical pollution concludes this paper. A twin paper (Escorza et al., 2019) addresses the same questions for dwarf barium stars.

## 2. Samples of barium and S stars without Tc

The present study is a follow-up of the monitoring campaign of barium and S stars initiated in 1984 with the CORAVEL spectrograph (Baranne et al., 1979), and whose results were presented in Jorissen & Mayor (1988, 1992), Jorissen et al. (1998), and Udry et al. (1998a,b).

The CORAVEL monitoring was not able to derive all the orbits either because several turned out to be much longer than its time span, or because its precision (about  $0.3 \text{ km s}^{-1}$ ) was not good enough to detect the orbits with the smallest semi-amplitudes (like  $0.6 \text{ km s}^{-1}$  for HD 183915 and HD 189581, as we will report in Sect. 4.3). These shortcomings motivated the pursuit of this former monitoring campaign after several years of interruption, with a spectrograph (HERMES, as described in Sect. 3) much more accurate than the old CORAVEL. The new monitoring, described in e.g., Van Winckel et al. (2010) and Gorlova et al. (2013), could thus reveal binary systems with much lower velocity amplitudes, not accessible to CORAVEL.

The sample comprises all 37 barium stars with strong chemical anomalies (dubbed Ba3, Ba4, or Ba5 in Warner scale; Warner, 1965) from the list of Lü et al. (1983), as well as 40 among the mild<sup>1</sup> barium stars of that list. Although the latter sample is by no means complete, it provides a good comparison to the (complete) sample of strong barium stars.

<sup>1</sup> See Table 8 in Sect. 9 for a rough calibration of the qualifications mild/strong in terms of quantitative s-process overabundances. There we show that  $[\text{La}/\text{Fe}]$  and  $[\text{Ce}/\text{Fe}]$  values of 1 dex fairly represent the transition between mild and strong barium stars. Conversely, no mild barium stars are found with  $[\text{Ce}/\text{Fe}]$  values below 0.2 dex.

The sample of barium stars monitored by HERMES comprises

- 2 strong barium stars (HD 123949, HD 211954) with long and uncertain orbital periods. All such properties mentioned here refer to the status at the start of the HERMES monitoring;
- 1 strong barium star with no evidence for binary motion (HD 65854);
- 11 mild barium stars with long, uncertain periods (HD 22589, HD 53199, HD 196673), or with a lower limit on the period (HD 40430, HD 51959, HD 98839, HD 101079, HD 104979, HD 134698, HD 165141, BD  $-10^\circ 4311$ );
- 3 suspected binaries (HD 18182, HD 183915, HD 218356) among mild barium stars, and 3 mild barium stars with no evidence for binary motion (HD 50843, HD 95345, HD 119185).

The S-star sample monitored by HERMES is constructed as follows:

- 6 stars (HD 30959 =  $\sigma^1$  Ori, HD 184185, HD 218634, HDE 288833, BD+31°4391, and BD+79°156) with a lower limit on the orbital period from Table 3a of Jorissen et al. (1998);
- 2 stars with no Tc lines and no evidence for binarity (BD  $-21^\circ 2601$  and HD 189581) from Table 3c of Jorissen et al. (1998);
- 4 poorly-studied symbiotic S stars not present in the original sample of Jorissen et al. (1998): Hen 4-18, V420 Hya, and ER Del from Van Eck & Jorissen (2002) and HR 363 from Jorissen et al. (1996).

To these twelve S stars monitored by HERMES, 22 supplementary systems with orbital elements already obtained by CORAVEL (as listed in Table 3a of Jorissen et al., 1998) must be added. In total, the sample of S stars monitored thus comprises 34 objects.

The sample of barium and S stars is listed in Sect. 4.3 (Table 4).

## 3. Radial-velocity monitoring with the HERMES spectrograph

The radial-velocity (RV) monitoring was performed with the HERMES spectrograph attached to the 1.2m Mercator telescope from the Katholieke Universiteit Leuven, installed at the Roque de los Muchachos Observatory (La Palma, Spain). The spectrograph began regular science observations in April 2009, and is fully described in Raskin et al. (2011). The fibre-fed HERMES spectrograph is designed to be optimised both in stability as well as in efficiency. It samples the whole optical range from 380 to 900 nm in one shot, with a spectral resolution of about 86 000 for the high-resolution science fibre. This fibre has a 2.5 arcsec aperture on the sky and the high resolution is reached by mimicking a narrow slit using a two-sliced image slicer.

The MERCATOR-HERMES combination is precious because it guarantees regular telescope time. This is needed for our monitoring programme and the operational agreement reached by all consortium partners (KU Leuven, Université libre de Bruxelles, Royal Observatory of Belgium, Landessternwarte Tautenburg) is optimised to allow efficient long-term monitoring, which is indispensable for this programme. The long-term monitoring of barium and S stars is performed within the framework of this HERMES consortium, with some further data points

acquired during KULeuven observing runs (Van Winckel et al., 2010; Gorlova et al., 2013). In total, about 200 nights/year are devoted to such a monitoring, and the observation sampling is adapted to the known variation time scale.

A Python-based pipeline extracts a wavelength-calibrated, cosmic-ray cleaned spectrum. A separate routine is used for measuring RVs, by means of a cross-correlation with a spectral mask constructed on an Arcturus spectrum. A restricted region, covering the range 478.11 – 653.56 nm (orders 55 – 74) and containing 1543 useful spectral lines, was used to derive the RV, in order to avoid tellurics lines on the red end, and often poorly-exposed and crowded spectrum on the blue end. A spectrum with a signal-to-noise ratio of 20 is usually sufficient to obtain a cross-correlation function (CCF) with a well-defined minimum. An example of CCF is shown in Fig. 1 of Jorissen et al. (2016).

A Gaussian fit is performed on the CCF, and delivers an internal precision of less than  $10 \text{ m s}^{-1}$  on the position of the centre (depending on the CCF shape). The absolute precision of a single RV measurement is  $\sim 200 \text{ m/s}$ , limited by the pressure fluctuations during the night in the spectrograph room (see Fig. 9 of Raskin et al., 2011). However, this drift has no effect if the arc spectrum used for wavelength calibration is taken consecutive to the science exposure. The long-term accuracy (i.e., over several years) may be estimated from the stability of the RV standard stars monitored along with the science targets. These standard stars are taken from the list of Udry et al. (1999), available at <http://obswww.unige.ch/~udry/std/std.html>. The distribution of the standard-star velocity standard deviations peaks at  $\sigma(Vr) = 55 \text{ m s}^{-1}$  (as shown in Fig. 2 of Jorissen et al., 2016), which may thus be adopted as the typical uncertainty on the radial velocities over the long term.

On the other hand, the difference between the standard-star-catalogue velocity and the measured value is on average  $4 \text{ m s}^{-1}$  with a standard deviation of  $109 \text{ m s}^{-1}$ . This difference of  $4 \text{ m s}^{-1}$  indicates that there is no zero-point offset between HERMES and Udry et al. (1999) list of standard velocity stars. The standard radial-velocity stars from Udry et al. (1999) are tied to the ELODIE velocity system (see Udry et al. 1999 for more details), but the CORAVEL radial velocities used here are on the old CORAVEL system, before its conversion to the ELODIE system. Hence, a zero-point offset needs to be applied to these old measurements in order to bring them on the ELODIE/HERMES system. However, because this zero-point offset is not easy to predict accurately since it depends on both the star's velocity and colour, its value was usually derived a posteriori by ensuring minimal orbital residuals. The applied offset is given in the caption of the figures displaying the orbital solutions (Figs. A.4, B.1–B.27).

## 4. Results of the radial-velocity monitoring

### 4.1. Binary frequency

This section reviews the binary frequency for barium and (extrinsic) S stars. It updates our previous review (Jorissen et al., 1998) with the new results from the HERMES monitoring. Our 1998 review concluded that 35 out of 37 barium stars with strong chemical anomalies showed evidence for being binary systems, 34 out of 40 for mild barium stars (plus an additional 3 stars with binary suspicion), and 25 out of 27 for Tc-poor S stars.

The present situation is summarized in Table 1, which includes as well stars monitored by McClure at the Dominion Astrophysical Observatory (McClure et al., 1980; McClure, 1983; McClure & Woodsworth, 1990).

For S stars, the two stars (HD 189581 and BD  $-21^\circ 2601$ ) previously lacking evidence for orbital motion now reveal their binary nature, thanks to the more accurate HERMES data (see Fig. A.1 for BD  $-21^\circ 2601$  and Fig. B.18 for HD 189581).

All barium stars monitored with HERMES (but one, HD 95345, as discussed below) now show clear signatures of binarity, although not all of them have orbits available yet. For instance, HD 50843 and HD 65854 are clearly long-period binaries of small amplitude (Figs. A.2 and A.3), irrespective of the uncertain zero-point offset, since the HERMES data alone reveal a clear drift. There is not enough data yet to look for an orbital solution, though.

The situation is not as clear for HD 95345, since there is a short-period, low-amplitude orbit possibly fitting the HERMES data points (Bottom panel of Fig. A.4 and Table 4). Assuming that there is no long-term trend, an offset of  $0.6 \text{ km s}^{-1}$  is needed to bring the old CORAVEL measurements in agreement with the new HERMES ones (this offset has been applied in the upper panel of Fig. A.4).

HD 19014 is a star monitored by the southern CORAVEL (Udry et al., 1998a) but not by HERMES (because it is located too far south). Evidence for binarity is nevertheless provided by the comparison of the old CORAVEL velocities, yielding an average velocity of  $13.3 \pm 0.11 \text{ km/s}$  (Table 2b of Jorissen et al., 1998), with the Gaia DR2 velocity of  $15.98 \pm 0.17 \text{ km/s}$  (Gaia Collaboration et al., 2018). There is thus a difference of  $2.7 \text{ km/s}$  between the two data sets. As we now discuss, the zero-point offset between CORAVEL and Gaia DR2 is unlikely to be so large, so that HD 19014 may be considered a binary star.

To assess the reliability of the above comparison between Gaia DR2 and CORAVEL velocities, we performed the same comparison for the supposedly constant star HD 95345 described above. Gaia DR2 yields  $6.2 \pm 0.2 \text{ km/s}$ , in perfect agreement with the HERMES and CORAVEL results (after applying the  $+0.6 \text{ km/s}$  offset to the latter; see top panel of Fig. A.4). This comparison thus confirms that the CORAVEL/Gaia-DR2 offset should not be larger than a few tenths of  $\text{km/s}$ .

It is interesting to extend this comparison to the stars HD 50843 and HD 65854, for which HERMES data reveal a low-amplitude, long-term drift. For them, Gaia DR2 yields  $13.95 \pm 0.15$  and  $0.82 \pm 0.17 \text{ km/s}$ , respectively, as compared to the HERMES values of  $\sim 13.7$  and  $\sim 0.8 \text{ km/s}$  (Figs. A.2 and A.3). Again, they are seen to agree within a few tenths of  $\text{km/s}$ , despite the long-term drifts.

### 4.2. Individual radial velocities

The individual radial velocities, referred to the barycentre of the solar system (from IRAF *astutils* routine using the Stumpff 1980 ephemeris), are presented in Tables 2 (for barium stars) and 3 (for S stars). The CORAVEL radial velocities (described in the papers by Udry et al., 1998a,b) used to compute the orbital solutions are repeated here.

The data before JD 2 455 000 are from the CORAVEL monitoring (Jorissen & Mayor, 1988; Jorissen et al., 1998), and the more recent data are from HERMES (Van Winckel et al., 2010; Gorlova et al., 2013). No zero-point correction has been applied to the data listed in Tables 2 and 3.

As discussed in Sect. 3, the HERMES radial velocities are tied to the ELODIE system, defined by the RV standard stars of Udry et al. (1999), while the CORAVEL data are still on the old (pre-1999) CORAVEL system.

**Table 1.** Updated binary frequency among barium and S star samples from Jorissen et al. (1998). S stars with radial-velocity jitter were not included. SB19 and SB98 stand for the number of spectroscopic binaries known in 2019 (present paper) and in 1998 (before HERMES), respectively, SBO denotes spectroscopic binaries with either good or preliminary orbits, SB stands for spectroscopic binaries with no orbit available yet, and SB? stands for suspected spectroscopic binary.

Class	N	SB19	SB98	SBO			SB	SB?	no evidence SB	New HERMES SBO
				total	good	preliminary				
Strong Barium (Ba 3,4,5)	37	37	35	36	36	0	1 <sup>a</sup>	0	0	2
Mild Barium (Ba 1,2)	40	40	34	37	32	5	2 <sup>b</sup>	1 <sup>c</sup>	0	15
S (no Tc)	34	34	25/27	32	29	3	2 <sup>d</sup>	0	0	14

Notes: (a) HD 19014 (b) HD 50843, HD 65854 (c) HD 95345 (d) BD -21°2601, T Sgr

**Table 2.** Individual radial velocities for barium stars. No offset is applied. The full table is only available as online material.

JD	V <sub>r</sub> (km s <sup>-1</sup> )	ε(V <sub>r</sub> ) (km s <sup>-1</sup> )	COR/HER
HD 40430			
2446741.638	-24.41	0.34	COR
2446822.392	-25.30	0.35	COR
2447248.326	-24.69	0.37	COR
2447458.685	-25.32	0.34	COR
2447563.359	-24.52	0.32	COR
2447855.578	-25.12	0.33	COR
2448202.658	-24.80	0.35	COR
2448334.329	-23.69	0.37	COR
2448586.603	-23.70	0.33	COR
2448649.381	-23.65	0.35	COR
2449058.317	-23.58	0.40	COR
2449373.343	-23.32	0.35	COR
2450354.640	-22.40	0.30	COR
2450384.662	-22.96	0.32	COR
2450461.412	-22.13	0.33	COR
2455167.549	-22.87	0.04	HER
2455199.512	-22.87	0.04	HER
2455222.414	-22.70	0.04	HER
2455497.708	-22.36	0.04	HER
2455662.351	-22.26	0.04	HER
2455809.689	-22.03	0.04	HER
2455842.755	-22.01	0.04	HER
2455910.585	-22.10	0.04	HER
2455936.513	-21.99	0.04	HER
2455954.400	-21.98	0.04	HER
2456012.368	-21.95	0.04	HER
2456307.447	-21.78	0.04	HER
2456383.389	-21.76	0.04	HER
2456566.673	-21.59	0.04	HER
2456191.701	-21.71	0.05	HER

#### 4.3. Orbits

The orbital elements of the newly derived orbits are listed in Table 4. Some among these are not well constrained yet. For barium stars, these are HD 18182, HD 104979, HD 119185, HD 134698, and HD 199394. Among S stars, HD 184185, HD 218634 (57 Peg), and HDE 288833 have poorly constrained orbital elements. All figures with the orbital solution superimposed on the radial-velocity data are presented in Appendix B. The orbital elements derived earlier may be found in Jorissen et al. (1998) and Udry et al. (1998a,b).

Before proceeding to the analysis of this orbital material in Sects. 6 and 7, we hereafter comment on individual stars.

## 5. Stars of special interest

### 5.1. HD 22589, HD 120620, HD 216219, and BD -10°4311

Although for backward compatibility, we kept HD 22589, HD 120620, HD 216219, and BD -10°4311 in the binary statistics of our original sample of (giant) barium stars (Table 1), the analysis of the Gaia Hertzsprung-Russell diagram (Escorza et al., 2017) reveals that these stars are dwarf barium stars instead (see Fig. 7 of Escorza et al., 2019). Further discussion of these stars is therefore presented in the companion paper about dwarf barium stars (Escorza et al., 2019).

### 5.2. o1 Ori (= HD 30959)

The star o1 Ori is peculiar in many respects. First, it is one of the few S stars with a direct detection of the WD companion from the *International Ultraviolet Explorer* (IUE; Ake & Johnson, 1988; Johnson et al., 1993)<sup>2</sup>. But o1 Ori is as well Tc-rich (Smith & Lambert, 1988, and bottom panel of Fig. 1), and as written by Ake & Johnson (1988), *this star is clearly something of an anomaly in showing Tc lines*, since it hosts as well a WD companion, and could therefore be considered as an extrinsic S star. Simple considerations about the implied time scales (as explained below) make it more likely however that o1 Ori is a unique example of an intrinsic-extrinsic S star! In other words, this star must have recently entered the thermally-pulsing AGB phase, responsible for the Tc production, adding to the possible former s-process pollution from the now extinct AGB companion.

Since the half-life of <sup>99</sup>Tc, the isotope of Tc involved in the s-process, is  $2.11 \times 10^5$  yr, the presence of Tc on the stellar surface indicates that less than  $10^6$  yr (i.e., a few half-lives) have elapsed since the last episode of Tc deposition on the surface. This constraint must be compared to the cooling time of  $10^8$  yr for a white dwarf with  $T_{\text{eff}} = 22\,000$  K (Salaris et al., 2013), as observed for o1 Ori. As these time scales are mutually incompatible, there is no possibility that the Tc now present on the M/S star was transferred from the companion while it was still an AGB star. The location of o1 Ori in the Hertzsprung-Russell

<sup>2</sup> The title of the paper by Ake & Johnson (1988) reads *A white dwarf companion to the main-sequence star 4 Omicron1 Orionis and the binary hypothesis for the origin of peculiar red giants*. We met H. Johnson soon after his paper was published by *The Astrophysical Journal*, and he confessed that the language editor had changed the MS letters standing for the spectral type, as originally present in the title, into 'main sequence', a change which of course turned the title into astrophysical nonsense! To avoid this ambiguity, we shall use the terminology M/S to denote a star intermediate between M- and S-spectral types.

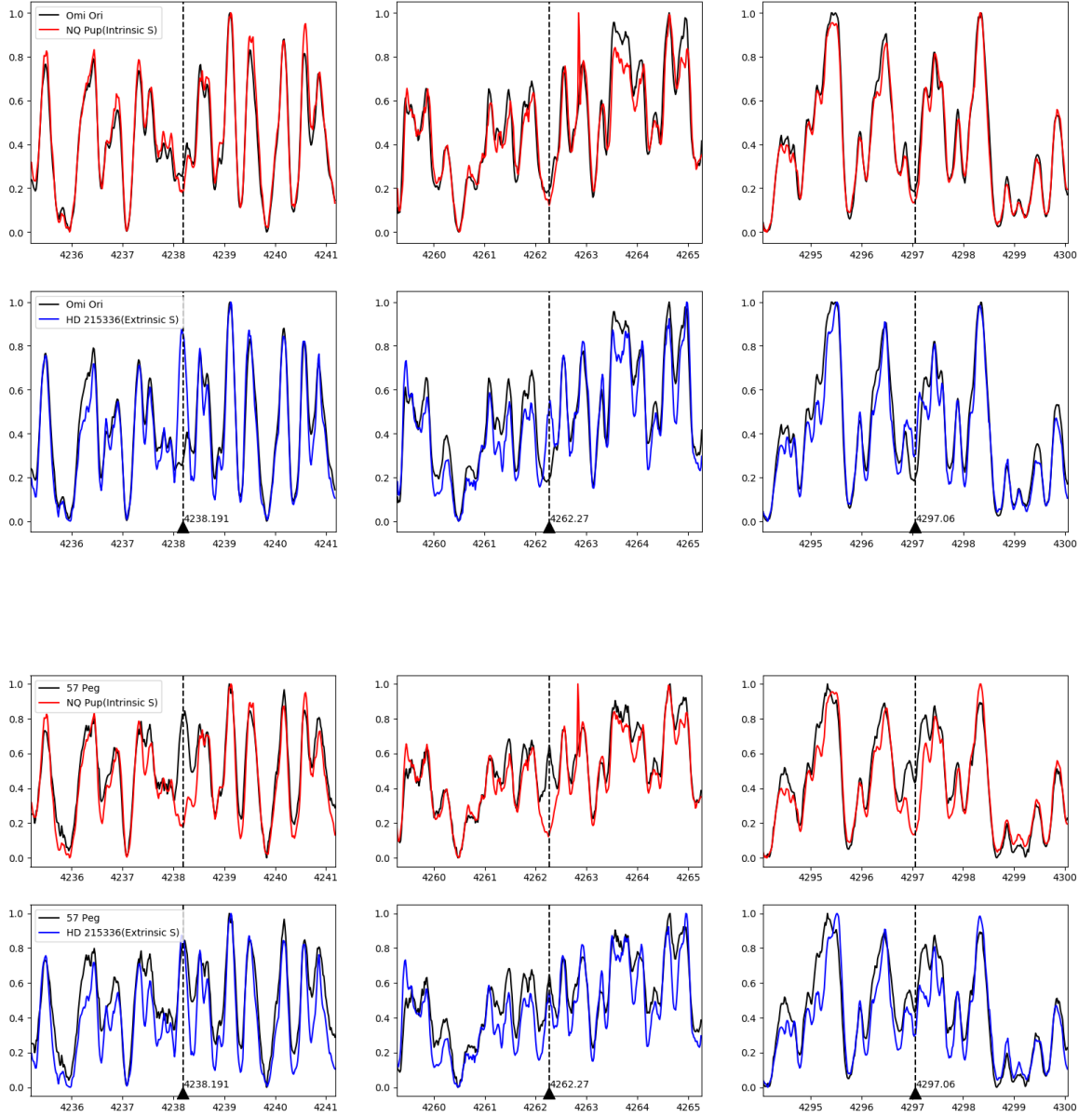


**Fig. 1.** The spectral regions around the Tc I  $\lambda$  423.82 nm (left column), 426.23 (middle column) and 429.71 lines (right column). *o1 Ori* (black line) is compared to an intrinsic S star (NQ Pup; red line; first row) and to an extrinsic S star (HD 215336; blue line; second row), from HERMES spectra. Third and fourth rows: same as first and second rows, but for 57 Peg compared to the same intrinsic and extrinsic S stars.

diagram, just at the onset of the thermally-pulsing AGB<sup>3</sup> (see Fig. 6 of Van Eck et al., 1998, confirmed by Gaia DR2, since the Hipparcos and Gaia DR2 parallaxes are mutually consistent:  $\varpi = 6.0 \pm 0.9$  and  $6.2 \pm 0.4$ , respectively), confirms the intrinsic nature of *o1 Ori*, i.e., it is an S star on the TP-AGB capable of producing Tc in its interior and bringing it to the surface. But it still raises the question of the origin (intrinsic or extrinsic?) of the s-process enhancement which confers *o1 Ori* its distinctive status as an M/S star. An important clue in that respect comes from the Nb/Zr chronometer (Neyskens et al., 2015; Karinkuzhi

et al., 2018), and from the orbital elements. In particular, is the system close enough to make the s-process pollution through mass transfer efficient?

To address the first question (intrinsic vs. extrinsic s-process?), a basic abundance analysis of *o1 Ori* has been performed, following the guidelines presented in Shetye et al. (2018), using the same iron and s-process lines, and the same procedure to select the model parameters among the large MARCS grid of S-star model atmospheres (Van Eck et al., 2017). The adopted model parameters for *o1 Ori* are listed in Table 5, and these parameters have been validated by the good match between observed and synthetic spectra around CH, Fe

<sup>3</sup> See Shetye et al. (2018, 2019) for other examples of Tc-rich S stars located just at the onset of the TP-AGB.

**Table 3.** Same as Table 2 for S stars. The full table is only available as online material.

JD	$V_r$ (km s <sup>-1</sup> )	$\epsilon(V_r)$ (km s <sup>-1</sup> )	COR/HER
HD 7351 = HR 363			
2443026.629	6.0	0.8	
2445340.328	-3.73	0.32	COR
2445343.266	-4.21	0.33	COR
2445595.607	-4.62	0.31	COR
2446008.492	-1.86	0.31	COR
2446015.452	-1.98	0.30	COR
2446296.568	-1.65	0.34	COR
2446335.598	-0.56	0.31	COR
2446715.530	0.87	0.33	COR
2446722.515	2.10	0.32	COR
2447097.429	2.23	0.34	COR
2447101.474	2.90	0.31	COR
2447459.489	4.20	0.31	COR
2447463.491	4.96	0.30	COR
2447867.364	6.42	0.31	COR
2447872.324	6.28	0.30	COR
2448128.588	7.10	0.30	COR
2448261.351	7.58	0.38	COR
2448671.272	5.68	0.32	COR
2448676.260	5.77	0.31	COR
2448936.527	2.36	0.30	COR
2448967.359	2.65	0.30	COR
2448972.435	2.68	0.34	COR
2449002.293	2.51	0.30	COR
2449313.423	0.15	0.30	COR
2449317.376	0.75	0.29	COR
2449321.403	0.54	0.34	COR
2449371.258	0.21	0.31	COR
2449639.675	-3.09	0.28	COR
2449640.558	-2.98	0.30	COR
2449730.266	-3.54	0.28	COR
2449734.264	-4.01	0.27	COR
2449781.273	-4.54	0.38	COR
2449783.266	-4.70	0.32	COR
2449785.273	-4.57	0.35	COR
2449964.601	-4.08	0.31	COR
2450042.373	-3.61	0.30	COR
2450052.367	-3.55	0.29	COR
2450072.276	-3.89	0.31	COR
2450083.366	-3.18	0.32	COR
2450123.246	-3.41	0.30	COR
2450325.584	-3.75	0.31	COR
2450355.449	-4.29	0.30	COR
2450363.445	-5.20	0.29	COR
2450382.356	-4.31	0.30	COR
2450415.473	-2.81	0.29	COR
2450420.398	-2.59	0.31	COR
2450428.330	-3.79	0.30	COR
2450476.308	-1.70	0.30	COR
2450615.617	-2.01	0.30	COR
2455039.709	-3.05	0.244	HER
2456488.655	4.81	0.247	HER
2456564.675	5.35	0.249	HER
2456565.708	5.41	0.249	HER
2456664.397	4.73	0.246	HER
2456271.531	1.81	0.254	HER
2456470.726	4.33	0.265	HER
2456833.719	4.95	0.253	HER
2456905.655	5.51	0.054	HER
2456907.617	5.60	0.053	HER
2456934.547	5.67	0.056	HER
2456947.552	6.91	0.054	HER
2457033.380	6.77	0.061	HER
2457208.638	6.12	0.054	HER
2457208.641	6.12	0.054	HER

and Zr lines. Fig. 2 for instance illustrates this good match around a Zr I line.

Table 5 presents the abundances derived in *o1 Ori* for elements C, N, Fe, Y, Zr, Nb, Ba, and Nd. The specific MARCS model atmosphere selected for *o1 Ori* is validated *a posteriori* by the agreement between the [Fe/H] and [s/Fe] values for the adopted MARCS model and those derived from the detailed abundance analysis (more precisely, they differ by less than one step in the model grid for both [Fe/H] and [s/Fe]). Comparing the [Nb/Fe] and [Zr/Fe] abundances in *o1 Ori* with those observed in extrinsic and intrinsic S stars (Neyskens et al. 2015; also Fig. 14 of Karinkuzhi et al. 2018; Fig. 15 of Shetye et al. 2018) very clearly points towards an intrinsic origin of the *o1 Ori* s-process abundances. The small [Nb/Fe] value indeed indicates that <sup>93</sup>Zr had no time yet to decay into the only stable Nb isotope, <sup>93</sup>Nb. Overall, the overabundance in s-process elements in *o1 Ori* is very moderate, with even some negative [X/Fe] values.

As far as the latter question (has s-process pollution through mass transfer been efficient?) is concerned, it could be answered by the knowledge of *o1 Ori* orbital elements. It has, however, been very difficult to extract an orbital signal from the long-term radial-velocity monitoring, because the amplitude of variations is small (2 to 3 km s<sup>-1</sup>) and there seems to be some velocity jitter (Fig. 3). This jitter could be associated with the envelope semi-regular pulsations with periods of 30.8 and 70.7 d, and amplitudes 0.047 and 0.046 mag, respectively (Tabur et al., 2009). Using Eq. 5 of Kjeldsen & Bedding (1995) rewritten as Eq. 6 of Jorissen et al. (1997) to relate photometric and radial-velocity jitter, a radial-velocity amplitude of 0.75 km s<sup>-1</sup> is predicted to be associated with a photometric visual amplitude of 0.047 mag (adopting  $T_{\text{eff}} = 3500$  K for *o1 Ori*; Table 5), in reasonable agreement with the data (bottom panel of Fig. 3).

An orbital solution may be obtained only after discarding data points obtained prior to 2012.7 (red crosses on Fig. 3). But even doing so, the  $O - C$  residuals remain large [ $\sigma(O - C) = 0.44$  km s<sup>-1</sup>; bottom panel of Fig. 3]. The mass function is indeed the second smallest of those reported in Table 4, at  $(2.7 \pm 0.2) \times 10^{-5} M_{\odot}$ . As we show below, this small mass function is very likely due to a small inclination angle on the plane of the sky.

Ake & Johnson (1988) fit the IUE spectrum of *o1 Ori* B with a WD model of  $\log g = 8$ , which according to Burleigh et al. (1997) corresponds to a mass of 0.65  $M_{\odot}$  and a radius of 0.014  $R_{\odot}$  for the WD (however, Ake & Johnson 1988 do not exclude that the gravity might be slightly larger, with  $\log g = 8.5$  then resulting in a mass of 0.96  $M_{\odot}$ ). Moreover, Cruzalèbes et al. (2013) have performed a detailed analysis of *o1 Ori* using AMBER/VLTI data. They obtained an angular diameter of  $9.78 \pm 0.10$  mas for that star, which, combined with the Gaia DR2 (DR2; Gaia Collaboration et al., 2016, 2018) parallax of  $6.2 \pm 0.4$  mas, yields a radius of  $170 \pm 14 R_{\odot}$ . Combining this radius with the effective temperature of 3500 K, a luminosity of 3900  $L_{\odot}$  ensues. Given the [Fe/H] = -0.5 metallicity of *o1 Ori* (Table 5), the above parameters locate the star on the evolutionary track of a 2 – 2.5  $M_{\odot}$  star according to Fig. 16 of Shetye et al. (2018). Inserting these masses and their uncertainties in the orbital mass function, we obtain an inclination on the order of only  $\sim 3.7^{\circ} - 5.7^{\circ}$  on the plane of the sky.

Combining the above mass estimates with the orbital period of 575 d (Table 4), one finds a relative semi-major axis in the range 1.9 – 2.0 au or 404  $R_{\odot}$ . The corresponding Roche radius around the giant component is then on the order of 184 – 235  $R_{\odot}$ , corresponding to a filling factor on the order of 72 – 92% for the observed radius of  $170 \pm 14 R_{\odot}$ . Orbital and diameter data thus indicate that *o1 Ori* is a detached system, possi-

**Table 4.** New, revised, and preliminary orbital elements (the latter data are followed by “:”).

HD/DM	Period (d)	$e$	$V_\gamma$ (km/s)	$T_0$	$K$ (km/s)	$\omega$ ( $^\circ$ )	$a_1 \sin i$ (Gm)	$f(m)$ ( $M_\odot$ )	$\sigma(\text{O-C})$ (km/s)	$N$
<b>Mild Ba stars</b>										
18182	8059:	0.3:								
40430	5609 $\pm$ 55	0.22 $\pm$ 0.01	-23.27 $\pm$ 0.04	2463116 $\pm$ 80	1.67 $\pm$ 0.06	88 $\pm$ 5	126 $\pm$ 7	0.0025 $\pm$ 0.0004	0.31	36
51959	9718 $\pm$ 157	0.53 $\pm$ 0.04	38.21 $\pm$ 0.04	2458537 $\pm$ 113	0.92 $\pm$ 0.06	50 $\pm$ 5	104 $\pm$ 11	0.00047 $\pm$ 0.00014	0.23	64
53199	8314 $\pm$ 99	0.24 $\pm$ 0.01	23.6 $\pm$ 0.1	2448483 $\pm$ 117	3.3 $\pm$ 0.1	63 $\pm$ 3	364 $\pm$ 14	0.028 $\pm$ 0.003	0.09	51
95345	485?	0.3?								
98839 <sup>b</sup>	16471 $\pm$ 113	0.560 $\pm$ 0.005	0.13 $\pm$ 0.01	2451547 $\pm$ 17	3.86 $\pm$ 0.03	288.9 $\pm$ 0.7	724 $\pm$ 13	0.056 $\pm$ 0.002	0.41	143
101079	1565.8 $\pm$ 1.7	0.175 $\pm$ 0.005	-2.000 $\pm$ 0.007	2458486 $\pm$ 6	2.48 $\pm$ 0.02	139.9 $\pm$ 1.2	52.6 $\pm$ 0.4	0.00236 $\pm$ 0.00005	0.13	55
104979	19295:	0.1:								
119185	22065:	0.6:								
134698	10005:	0.95:								
183915	4382 $\pm$ 21	0.27 $\pm$ 0.02	-49.83 $\pm$ 0.01	2462214 $\pm$ 80	0.56 $\pm$ 0.01	130 $\pm$ 6	32.6 $\pm$ 0.8	(7.2 $\pm$ 0.5) <sup>-5</sup>	0.36	98
196673	7780 $\pm$ 117	0.59 $\pm$ 0.02	-24.2 $\pm$ 0.1	2451698 $\pm$ 128	3.7 $\pm$ 0.1	116 $\pm$ 2	314 $\pm$ 20	0.020 $\pm$ 0.003	0.40	75
199394	5232: <sup>d</sup>	0.11:								
<b>Strong Ba star</b>										
123949	8523 $\pm$ 8	0.9162 $\pm$ 0.0003	-9.56 $\pm$ 0.01	2466294 $\pm$ 8	9.33 $\pm$ 0.02	96.5 $\pm$ 0.2	438 $\pm$ 2	0.0462 $\pm$ 0.0005	0.20	86
211954	10889 $\pm$ 113	0.24 $\pm$ 0.05	-6.0 $\pm$ 0.5	2461595 $\pm$ 803	4.1 $\pm$ 0.8	357 $\pm$ 17	601 $\pm$ 137	0.07 $\pm$ 0.06	0.25	23
<b>S stars</b>										
7351	4596 $\pm$ 7	0.18 $\pm$ 0.01	1.67 $\pm$ 0.02	2444703 $\pm$ 20	5.38 $\pm$ 0.03	105.7 $\pm$ 1.4	334.4 $\pm$ 2.5	0.070 $\pm$ 0.001	0.64	76
170970	4651 $\pm$ 10	0.19 $\pm$ 0.01	-35.68 $\pm$ 0.03	2457482 $\pm$ 40	3.60 $\pm$ 0.03	234 $\pm$ 3	226 $\pm$ 3	0.0213 $\pm$ 0.0007	0.31	50
184185	15723:	0:								
189581	618 $\pm$ 1	< 0.02	-17.12 $\pm$ 0.01	2457037 <sup>e</sup>	0.59 $\pm$ 0.02	-	5.0 $\pm$ 0.2	(1.3 $\pm$ 0.1) $\times 10^{-5}$	0.36	52
215336	1143.6 $\pm$ 0.7	0.040 $\pm$ 0.009	-2.28 $\pm$ 0.05	2454855 $\pm$ 30	6.90 $\pm$ 0.02	188 $\pm$ 9	108.5 $\pm$ 0.1	0.03887 $\pm$ 0.00006	0.25	35
288833	28557:	0.35:								
218634 <sup>c</sup>	194313:	0.8:								
BD +79° 156	10921 $\pm$ 40	0.458 $\pm$ 0.004	-31.82 $\pm$ 0.04	2468051 $\pm$ 40	3.20 $\pm$ 0.04	186 $\pm$ 1	428 $\pm$ 8	0.026 $\pm$ 0.001	0.52	68
CD -28° 3719	397.5 $\pm$ 0.1	0.042 $\pm$ 0.002	65.18 $\pm$ 0.02	2457148 $\pm$ 4	7.84 $\pm$ 0.01	152 $\pm$ 3	42.83 $\pm$ 0.07	0.0198 $\pm$ 0.0001	0.75	27
BD +31° 4391	6748 $\pm$ 35	0.16 $\pm$ 0.02	24.0 $\pm$ 0.1	2457525 $\pm$ 91	3.0 $\pm$ 0.1	149 $\pm$ 6	280 $\pm$ 9	0.019 $\pm$ 0.02	0.47	62
ER Del	2081 $\pm$ 2	0.281 $\pm$ 0.003	-48.80 $\pm$ 0.01	2454427 $\pm$ 4	7.12 $\pm$ 0.03	116.8 $\pm$ 0.6	195.7 $\pm$ 0.3	0.0689 $\pm$ 0.0002	1.2	41
V420 Hya	751.4 $\pm$ 0.2	0.099 $\pm$ 0.004	-5.91 $\pm$ 0.05	2449838 $\pm$ 6	10.49 $\pm$ 0.03	271 $\pm$ 3	107.9 $\pm$ 0.4	0.089 $\pm$ 0.001	1.19	69
Hen 4-147	346.62 $\pm$ 0.04	0.112 $\pm$ 0.006	-5.2 $\pm$ 0.1	2454195 $\pm$ 4	12.3 $\pm$ 0.2	358 $\pm$ 4	58.2 $\pm$ 0.8	0.065 $\pm$ 0.003	0.26	45
$\sigma^1$ Ori	574.7 $\pm$ 1.5	0.22 $\pm$ 0.02	-9.79 $\pm$ 0.01	2457525 $\pm$ 6	0.79 $\pm$ 0.02	196 $\pm$ 4	6.1 $\pm$ 0.2	(2.7 $\pm$ 0.2) $\times 10^{-5}$	0.44	60

<sup>a</sup> Epoch of maximum velocity (circular orbit)<sup>b</sup> HD 98839 = 56 UMa<sup>c</sup> HD 218634 = 57 Peg<sup>d</sup> A solution with  $P = 10481$  d and  $e = 0.36$  is also possible. However, considering the unusual mass function of  $0.128 \pm 0.007 M_\odot$ , this solution is less likely than the shorter solution which has a more common mass function of  $0.030 \pm 0.001$ .<sup>e</sup> Epoch of maximum velocity.

bly with a large filling factor. Ellipsoidal variations are not expected, though, since the system appears to be seen almost face-on. However, in this case, a non-circular stellar disc could be detected by interferometry, using three non-aligned telescopes. The closure-phase parameter (CSP) may be used to measure the deviation from centrosymmetry of the stellar surface brightness distribution, as done by Cruzalèbes et al. (2015). The CSP relies on the triple product of the complex visibilities recorded by the three telescopes; its exact definition is beyond the scope of this paper, and we refer the interested reader to the paper by Cruzalèbes et al. (2014). Here, it suffices to say that CSP equals  $0^\circ$  or  $180^\circ$  for a central-symmetric surface brightness distribution. In  $\sigma^1$  Ori, there is a small deviation from centrosymmetry (CSP =  $8.1^\circ \pm 0.8^\circ$  instead of  $0^\circ$  in the central-symmetric case). However, this level of asymmetry could as well be caused by the convective pattern at the surface of this giant star (see Cruzalèbes et al., 2014; Paladini et al., 2014, for a discussion of convective vs. tidal asymmetries in giant stars). The CSP value for  $\sigma^1$  Ori

indeed lies at the expected position along the sequence of increasing convective asymmetries with increasing pressure scale-heights along the giant branch (see Figs. 4 and 6 of Cruzalèbes et al., 2015). Therefore, it is likely that  $\sigma^1$  Ori shows no sign of tidal deformation, so that its Roche-filling factor must be closer to 72% than to 92%; hence, the most likely masses are those corresponding to the filling factor of 72%, namely  $M_S = 2.5 M_\odot$  and  $M_{WD} = 0.65 M_\odot$ .

### 5.3. HD 98839 = 56 UMa

For HD 98839 (=56 UMa), we improve upon the orbit published by Griffin (2008a). Thanks to 25 new HERMES measurements spanning the years 2009 – 2016, as listed in Table 2, a full orbital cycle has now been covered for this barium star with an orbital period of  $45.1 \pm 0.3$  yr, one of the longest among barium and extrinsic S stars.



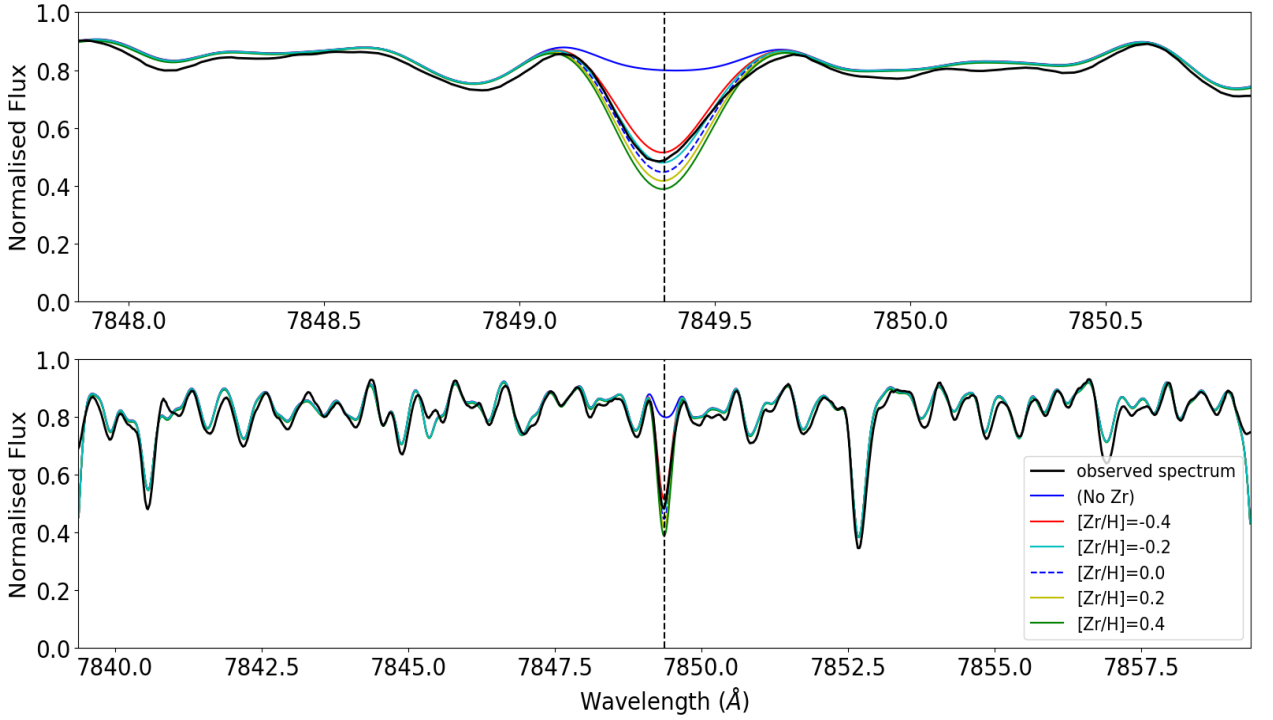


**Fig. 2.** Illustration of the quality of the match between observed and synthetic spectra obtained for the extrinsic S star *o*1 Ori around the Zr I line at 7849.37 Å. The upper panel presents a  $\pm 3$  Å zoom.

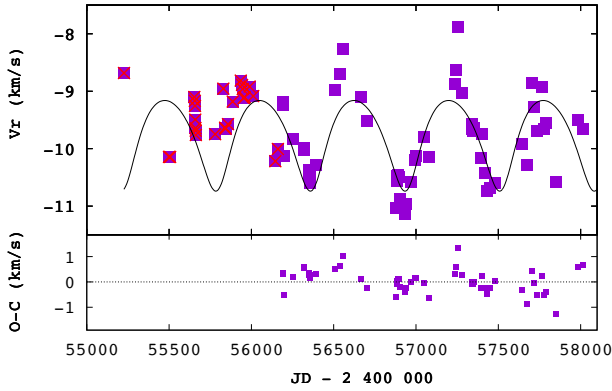


**Fig. 3.** The tentative orbit of *o*1 Ori, based on the magenta square points.

An offset of +0.6 km/s was applied to these HERMES measurements to put them in agreement with those used by Griffin for his orbital solution. Nevertheless, the systemic velocity listed in Table 4 has been converted back into the HERMES/IAU system to ensure consistency with the other orbital solutions. In our orbital solution (shown in Fig. B.5), we did not include measurements older than JD 2 440 000, because they degrade the orbit quality.

#### 5.4. HD 134698

HD 134698 has a very large eccentricity ( $e \sim 0.95!$ ), and it was not possible to converge to a solution taking into account all the old CORAVEL data points, as shown on Fig. B.10.

#### 5.5. HD 196673

HD 196673 is a visual double star (WDS 20377+3322) with a separation varying between 2.5'' in 1828 and 3.2'' in 2014. The B component is, according to the Gaia Data Release 2 (Gaia Collaboration et al., 2016, 2018), about one magnitude fainter than the barium star, and their  $B_p - R_p$  are similar (1.275 and 1.187 for A and B, respectively), as are their parallaxes ( $\varpi = 1.62 \pm 0.03$  mas). This indicates that AB is a pair of red giants, separated by  $\sim 1850$  au. Assuming a mass of  $1.5 M_{\odot}$  for both stars, an orbital period of  $5 \times 10^4$  yr ensues. One radial-velocity measurement of HD 196673B has been obtained (-25.5 km/s; Table 2), close to the systemic velocity of the Aa spectroscopic pair (-24.2 km/s; Table 4), further confirming that the visual pair is physical.

#### 5.6. T Sgr = HD 180196

The Tc-rich S star T Sgr has been included in the monitoring because the star is known to have a composite spectrum, with a F4 IV companion becoming visible near minimum light (Herbig, 1965; Culver & Ianna, 1975), and we hoped to detect the velocity drift associated with the orbital motion. However, as we explain below, despite 9 years of monitoring, there was no such drift clearly detected, suggesting that the pair must be quite wide.



**Table 5.** Abundances in the S stars *o*1 Ori (top panel) and 57 Peg (bottom panel). The column labeled *N* gives the number of lines used to derive the corresponding abundances. The uncertainty listed in the  $\log \epsilon_X$  column corresponds to the line-to-line scatter, whereas the one listed in column  $[X/Fe]$  is the root-mean-square of the former value and the uncertainty propagating from the model-atmosphere uncertainties, as estimated for V915 Aql by Shetye et al. (2018; their Table 8). V915 Aql has atmospheric parameters similar to those of *o*1 Ori and 57 Peg.

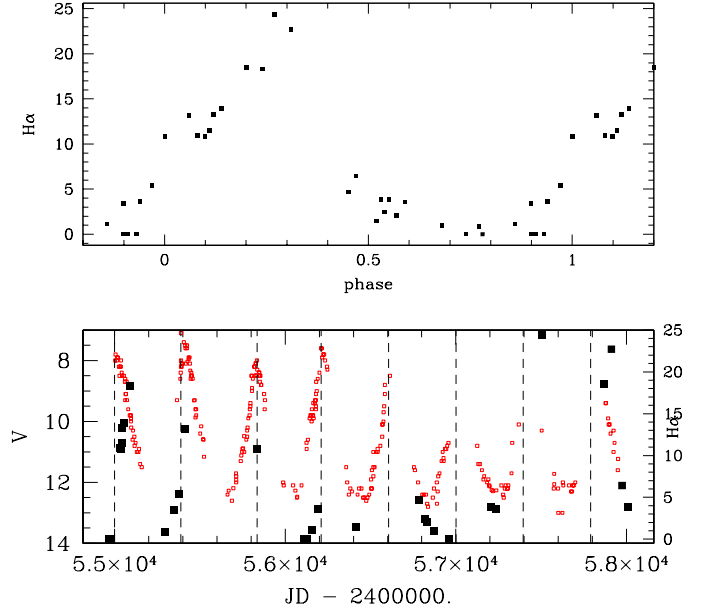
<i>o</i> 1 Ori					
MARCS model:					
$T_{\text{eff}} = 3500 \text{ K}$ , $\log g = 0.0$ , $[Fe/H] = -0.50$ , $C/O = 0.50$ , $[s/Fe] = 0.00$					
Z	X	$\log \epsilon_X$	$[X/H]$	$[X/Fe]$	<i>N</i>
6	C	8.06	-0.37	0.13	
7	N	7.4	-0.4	$0.07 \pm 0.63$	
26	Fe	$7.0 \pm 0.13$	-0.5	$\pm 0.16$	12
39	Y	$1.8 \pm 0.00$	-0.41	$0.09 \pm 0.00$	2
40	Zr	$2.45 \pm 0.07$	-0.13	$0.37 \pm 0.07$	2
41	Nb	$1.02 \pm 0.17$	-0.44	$0.06 \pm 0.17$	4
56	Ba	$1.8 \pm 0$	-0.4	$0.12 \pm 0.10$	1
60	Nd	$1.0 \pm 0$	-0.4	$0.08 \pm 0.20$	2

57 Peg					
MARCS model:					
$T_{\text{eff}} = 3400 \text{ K}$ , $\log g = 1.0$ , $[Fe/H] = 0.00$ , $C/O = 0.50$ , $[s/Fe] = 0.00$					
Z	X	$\log \epsilon_X$	$[X/H]$	$[X/Fe]$	<i>N</i>
6	C	8.16	-0.27	-0.07	
7	N	8.60	0.77	$0.97 \pm 0.63$	
26	Fe	$7.25 \pm 0.14$	-0.25	$\pm 0.17$	13
39	Y	$1.95 \pm 0.07$	-0.26	$0.04 \pm 0.07$	2
40	Zr	$2.45 \pm 0.21$	-0.13	$0.12 \pm 0.21$	2
56	Ba	$2.0 \pm 0$	-0.18	$0.07 \pm 0.10$	1
60	Nd	$1.4 \pm 0$	-0.02	$0.23 \pm 0.20$	2
62	Sm	$0.85 \pm 0.21$	-0.11	$0.14 \pm 0.21$	2

T Sgr is a Mira variable with a period of 394.7 d according to the *General Catalogue of Variable Stars* (v. 5.1; Samus' et al., 2017). This period is confirmed by the *Association of French Variable Star Observers* (AFOEV) which detected light variations with a period varying between 377 d (cycle 3) and 446 d (cycle 2) during the time span of the HERMES monitoring (Bottom panel of Fig. 4). The photometric phase was computed with an origin at JD 2454611, and using either the contemporaneous period (when it could be measured from the photometric data, for cycles 1–4) or the GCVS period of 395 d (cycles 5–8). The photometric phase is listed again in the right margin of Fig. 5, which shows the series of CCF obtained with a F0 template, ordered according to the photometric phase. Along the 8 photometric cycles covered, the CCFs have stayed remarkably similar at any given phase, thus showing no sign of orbital drift.

The Mira has a shock wave travelling through its photosphere around maximum light. This shock wave manifests as line doubling (between fractional phases -0.1 to 0.3; Fig. 5),



**Fig. 4.** Bottom panel: Light curve for the S star T Sgr (small red open squares on bottom panel), from the *Association of French Variable Star Observers* (AFOEV). The vertical dashed lines mark the light maxima, either directly identified on the light curve (the first four) or inferred from the GCVS period 394.7 d. The strength of the Balmer H $\alpha$  emission line peak value normalised with respect to the continuum) is represented as solid open squares to be read off the right scale. Top panel: The Balmer H $\alpha$  line strength as a function of the photometric phase.

a well-studied behaviour known as the Schwarzschild scenario (see Alvarez et al., 2000; Jorissen et al., 2016, for an illustration of that scenario at work in Mira variables). The red component, corresponding to infalling matter, is the only one present during fractional phases 0.7 – 0.9, and gives way to an increasingly stronger blue component, corresponding to rising matter. In T Sgr, these two peaks have velocities of about -13 and +7 km s<sup>-1</sup> (Table 6). At the same time, H $\alpha$  in emission gets stronger and stronger (Top panel of Fig. 4). In that figure, the number characterizing H $\alpha$  emission is simply  $[I_{\text{max}}(H\alpha) - I(\text{continuum})]/I(\text{continuum})$ .

Around phase 0.5 (minimum light), these double peaks give way to a broad single peak, and this feature is especially visible when performing the correlation of the observed spectrum with a F0 mask. The corresponding velocities are listed in Table 6, which reveals a drift, but its significance is weakened by the broadness of the CCF (on the order of  $\sigma \sim 15 \text{ km s}^{-1}$ , associated with a rotational velocity  $V_{\text{rot}} \sin i \sim 25 \text{ km s}^{-1}$ ). The Mira velocity peaks do not confirm this drift, although a supplementary complication here comes from the fact that the shock-wave velocity may vary from cycle to cycle.

We note as well that the F-star velocity falls almost exactly at mid-range between the two Mira peaks, which is surprising: either the two stars are now going through a conjunction on a very long orbit, or the velocity amplitude of their orbit is small (a few km s<sup>-1</sup>), or the broad CCF seen at minimum light is not at all related to the F star.

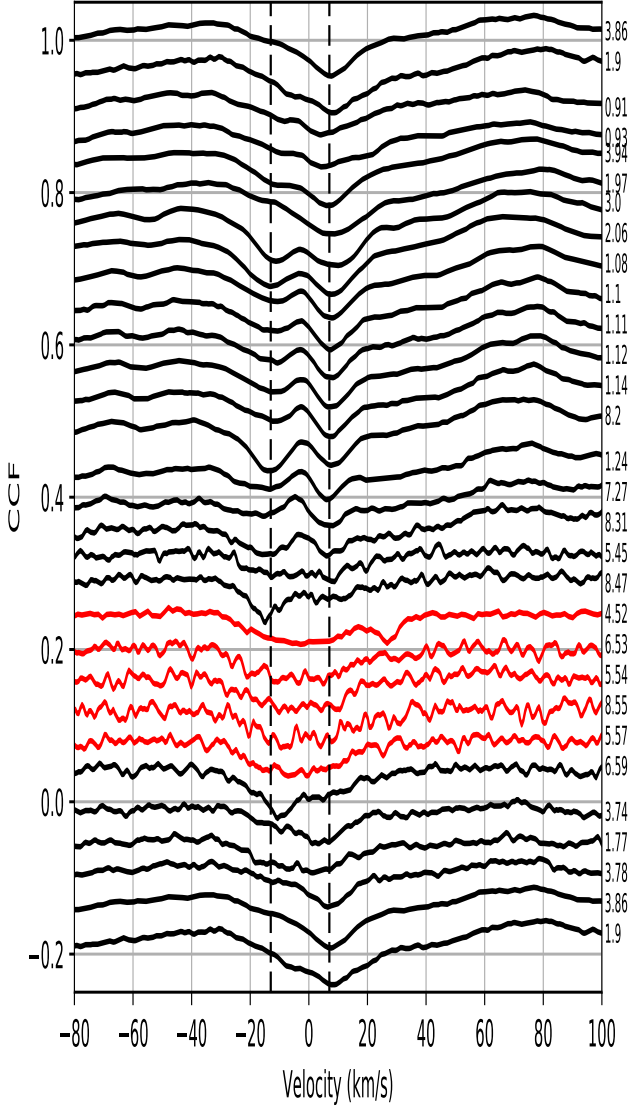


**Fig. 5.** The cross-correlation functions of the S star T Sgr (using mask F0) ordered according to (fractional) photometric phase, counted in cycles (as labelled in the right margin) since the light maximum at JD 2454611 (see Fig. 4). The vertical dashed lines mark the two peaks appearing in the Mira spectrum between phases -0.1 and 0.3, at velocities -13 and +7 km s<sup>-1</sup>. These peaks exhibit no noticeable orbital drift over the 9 years covered by the radial-velocity monitoring. The noisy CCFs between phases 0.5 and 0.6 (represented in red, and corresponding to the Mira minimum light) reveal a broad single peak, most likely belonging to the F companion, centered around -2 km s<sup>-1</sup>, and with a rotational broadening of about 25 km s<sup>-1</sup>.

### 5.7. HD 218634 = 57 Peg

The preliminary orbit of the S star 57 Peg (HD 218634) is standing out with its orbital period of the order of 500 yr (Table 4 and Fig. B.20), the longest period known so far for a chemically-peculiar red giant, and probably even among spectroscopic binaries as a whole (Griffin, 2008a). To better constrain it, it was necessary to add the old measurements from Griffin & Peery (1974). The period is not well constrained, and we do not exclude, however, that the orbital period will turn out to be shorter

**Table 6.** The radial velocities of the F and Mira components of the T Sgr system as a function of the photometric phase  $\phi$ , along with the  $\sigma$  of the CCF. The last columns list the velocities of the two peaks associated with the shock wave travelling in the Mira photosphere.

JD	$\phi$	$V_r$ (F) (km s <sup>-1</sup> )	$\sigma$ (CCF) (km s <sup>-1</sup> )	$V_{r1}$ (Mira) (km s <sup>-1</sup> )	$V_{r2}$ (Mira) (km s <sup>-1</sup> )
2455297.71	1.77	$-0.8 \pm 0.3$	16.3	-	-
2455413.57	2.06	-	-	$-13.9 \pm 0.1$	$8.3 \pm 0.1$
2456159.46	3.86	-	-	-	$6.9 \pm 0.2$
2456190.45	3.94	-	-	$-12.9 \pm 0.3$	$6.4 \pm 0.2$
2456416.70	4.52	$-1.8 \pm 0.4$	14.6	-	-
2456784.70	5.45	$-2.7 \pm 0.6$	20.5	-	-
2456817.65	5.54	$-3.2 \pm 0.4$	19.0	-	-
2456832.61	5.57	$-4.2 \pm 0.4$	15.0	-	-
2457208.54	6.53	$-3.8 \pm 0.5$	15.0	-	-
2457867.75	8.20	-	-	$-13.7 \pm 0.1$	$8.7 \pm 0.1$
2458008.39	8.55	$-2.7 \pm 0.5$	15.8	-	-

(100 yrs?; see the dashed line in Fig. B.20) when evaluated with measurements spanning a longer time interval.

The Tc-poor star 57 Peg (see bottom panel of Fig. 1) is special in many respects. First, it has a rather high luminosity ( $M_{\text{bol}} = -4.3$ , with a small uncertainty on its Hipparcos parallax  $\sigma_{\pi}/\pi = 0.21$ ; Hipparcos and Gaia DR2 parallaxes for 57 Peg are consistent with each other, with Gaia parallax only twice more precise:  $\sigma_{\pi}/\pi = 0.10$ ), and it falls along the  $Z = 0.2$  evolutionary track of a 3  $M_{\odot}$  star (Fig. 6 of Van Eck et al., 1998). Second, according to the detailed analysis of its UV colours presented in the Appendix of Van Eck et al. (1998), it has a composite spectrum with an A6V companion instead of the WD companion expected for extrinsic S stars in the framework of the binary paradigm. Adopting thus a mass of 1.9  $M_{\odot}$  for such an A6V companion yields a  $Q$  value of 0.286  $M_{\odot}$  [with  $Q = M_A^3/(M_S + M_A)^2$ ], assuming a mass of 3  $M_{\odot}$  for the S star. Incidentally, the S star primary must have evolved faster and should thus be more massive than 1.9  $M_{\odot}$ , which is consistent with its position along the 3  $M_{\odot}$  track in the HR diagram. Despite the fact that the orbit is not fully constrained yet, it yielded a mass function  $f(M_S, M_A) = 0.38 \pm 0.22 M_{\odot}$  compatible (within the error bars) with the above-predicted value for a 1.6  $M_{\odot}$  companion [since  $\sin^3 i = f(M_S, M_A)/Q$ , and therefore  $f(M_S, M_A)$  should be smaller than  $Q$ ]. However, a WD companion with a mass of 0.7  $M_{\odot}$ , which would yield  $Q = 0.025 M_{\odot}$ , seems incompatible with the observed mass function and the condition  $f(M_S, M_A) \leq Q$ . All evidence thus concurs towards the main-sequence nature of the companion. 57 Peg thus adds to the small set of Tc-poor S stars (HD 191589, HDE 332077) with a main sequence companion (Jorissen & Mayor, 1992; Ake & Johnson, 1992; Ake et al., 1994; Jorissen et al., 1998).

Faced with such strong evidence, possibilities to resolve this puzzle within the framework of the binary paradigm include (i) 57 Peg is a triple system (S+A6V+WD), or (ii) the companion is an accreting WD mimicking a main sequence spectrum, or (iii) 57 Peg is an intrinsic (Tc-rich) rather than Tc-poor S star, or finally (iv) 57 Peg is not an S star at all.

Possibility (i) is incompatible with the long-period orbit of the system, since a triple system needs to be hierarchical to be stable, with a period ratio on the order of 10. Since the 500-yr orbit is that of the main-sequence companion (as derived from the mass function), a 5000-yr orbit is implied for the WD com-

panion (a 50-yr orbit is not possible, since it would be detected first, having a larger velocity amplitude). But a 5000-yr orbit (corresponding to  $1.8 \times 10^6$  d) would never yield large enough pollution levels to transform the accretor into an extrinsic S star, since the longest orbital periods among our representative samples of extrinsic stars do not exceed  $4 \times 10^4$  d (see as well Fig. 15 showing how  $[s/Fe]$  decreases with increasing orbital periods).

Possibility (ii) is supported neither by the mass function (which calls for a genuine A6V star rather than a rejuvenated WD), nor by the IUE SWP spectrum which carries no sign of binary interaction (no C IV  $\lambda$  155.0 nm emission for instance).

Possibility (iii) is refuted by Fig. 1, which clearly demonstrates the Tc-poor nature of 57 Peg, based on a HERMES spectrum around the Tc I  $\lambda$  423.82 nm, 426.23, and 429.71 lines.

Possibility (iv) – that 57 Peg is not an S star – was already suggested by Smith & Lambert (1988). This hypothesis can be tested from an abundance analysis of the s-process elements in 57 Peg. For this purpose, we use an HERMES spectrum of 57 Peg obtained on September 6, 2009 (JD 2455080.640), with a signal-to-noise ratio of 150 in the V band. The atmospheric parameters of 57 Peg were derived following the method described by Van Eck et al. (2017) and Shetye et al. (2018). The adopted model parameters are listed in the bottom panel of Table 5. The abundance analysis has been performed using the same iron and s-process lines as in Shetye et al. (2018). We note especially that the lines used were located far enough in the red not to be contaminated by light from the A-type companion. Fig. 6 presents the good match between the synthetic and observed spectra around a Zr I line. Table 5 reveals that all the heavy elements studied have an abundance compatible with the solar-scaled value. The error bars quoted in column  $[X/Fe]$  of that table include, on top of the line-to-line scatter, the uncertainty propagating from the model-atmosphere uncertainties. The latter has been estimated by Shetye et al. (2018; their Table 8) for the S star V915 Aql and applied here to 57 Peg, since both stars have similar atmospheric parameters (same  $T_{\text{eff}}$  but  $\log g$  differing by 1 dex).

There is, however, a surprising N overabundance (larger than expected after the first dredge-up, if taken at face value; on that topic, see as well Karinkuzhi et al., 2018). Thus, our conclusion regarding 57 Peg is that this star has been misclassified as an S star, in line with Smith & Lambert (1988) suggestion.

## 6. The eccentricity - period diagram

With the addition of the new HERMES orbits to the existing sample (Jorissen et al., 1998; Van der Swaelmen et al., 2017), the number of giant barium and S stars with orbital elements available now amounts to 105 systems (36 strong Ba, 37 mild Ba, and 32 S stars). In the remainder of this paper, we analyse this rich data set, starting with the eccentricity-period ( $e - P$ ) diagram (Fig. 7). This diagram reveals distinctive features that may be used as benchmarks for binary-evolution models:

- The upper left threshold (represented by the dashed line in panel c of Fig. 7), due to tidal evolution or periastron mass transfer;
- The lower right gap (represented by the hatched area in Fig. 7), survival from initial conditions observed in young binaries like pre-main sequence stars;
- The existence of two populations: a population with (nearly) circular, short-period ( $P < 10^3$  d) orbits (almost exclusively found among strong barium stars), and a population of ec-

centric systems with intermediate ( $10^3 \leq P(d) \leq 10^4$ ) and very long periods ( $P > 10^4$  d).

- With all orbits now available, including the very long-period ones, we can state that the longest orbital period where s-process pollution through mass transfer may produce an extrinsic star is about  $4 \times 10^4$  d ( $\sim 110$  yr), since no system with a period longer than this value is found in our samples. This period however is the post-mass-transfer value, which certainly differs from the initial value. This maximum period provides an interesting constraint for binary mass-transfer models, which often predict the possibility of forming extrinsic systems with even longer periods (as long as a few  $10^5$  d; see Abate et al., 2015b, 2018, and references therein).

Extrinsic S stars (Panel d of Fig. 7) do not add new features or structure in the  $e - P$  diagram; they confirm the division of Ba stars in two populations in the  $e - P$  diagram. The maximum eccentricity at a given period is similar for barium and S stars (if one excepts the presence of two barium stars at  $P \sim 10^4$  d with large eccentricities –  $e > 0.9$ , with no equivalent among S stars, but this may result from small-number statistics). Extrinsic S stars are thus fully identical to barium stars orbit-wise.

The population of (almost) circular barium stars with  $P < 1000$  d is likely to contain objects that were circularised by tidal effects while the current barium star was ascending the first giant branch (supposing that most barium stars are currently located in the red-giant clump, as suggested by the analysis of their Hertzsprung-Russell diagram; Escorza et al., 2017). This circularisation process is posterior to and independent from the mass-transfer process. We justify the above statement by the fact that S stars, which are still on the RGB, are not yet fully circularised in the same period range, as indicated by the large clump of S stars observed around  $P \sim 700$  d and  $e \sim 0.08$ . A similar argument holds for the  $e - P$  diagram of post-AGB and dwarf barium stars, which include as well short-period non-circular systems (Oomen et al., 2018; Escorza et al., 2019). One may actually wonder why these short-period post-AGB, dwarf-barium and S systems are not circularised as they hosted in the past a large AGB star. Several authors argued that an as yet not fully identified process (periastron mass transfer, tidal interaction with a circumbinary disc, momentum kick associated with the white-dwarf formation?) must have been at work during the mass-transfer process to counteract the circularisation process and to pump the eccentricity up (Soker, 2000; Izzard et al., 2010; Dermine et al., 2013).

We stress moreover that the population of (almost) circular barium stars with  $P < 1000$  d is almost absent among mild barium stars (with the exception of HD 77247 and HD 218356). Therefore, there must be a link between the mass-transfer properties and the resulting s-process overabundances to account for the near absence of short-period systems among systems with mild s-process overabundances. This will be discussed further in Sect. 9. As a corollary, we note that HD 199939, with  $P = 585$  d and  $e = 0.28$ , is an outlier among strong barium stars, having a large eccentricity for its period (panel b of Fig. 7). Its orbital elements were obtained by McClure & Woodsworth (1990), and a closer look at their orbital solution does not reveal any anomaly (like the presence of a third companion) that could account for its outlying nature. Finally, we stress that the segregation between mild and strong barium stars, used to draw panels a and b of Fig. 7, although initially based on Warner’s visual index of the strength of the Ba II line (Warner, 1965), is generally confirmed by a detailed abundance analysis (as further discussed in Sect. 9). Adopting  $[La/Fe]$  and  $[Ce/Fe]$  values of 1 dex as thresh-

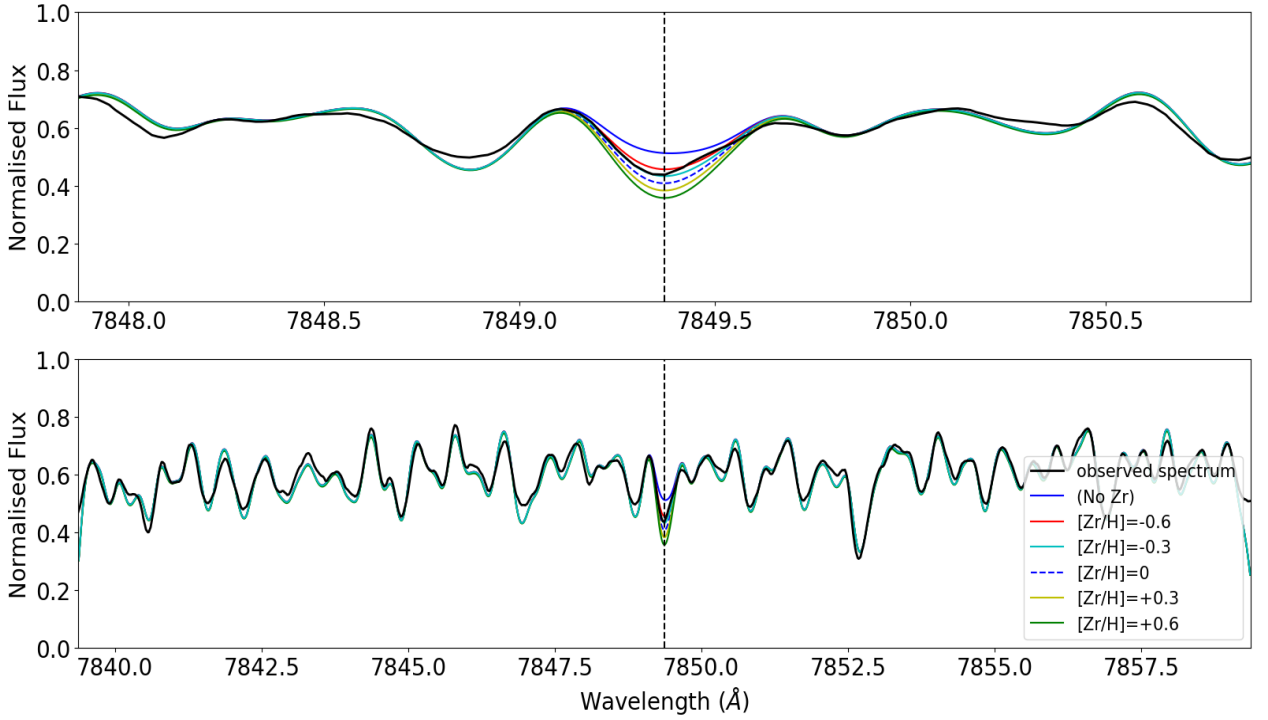


**Fig. 6.** Same as Fig. 2 for 57 Peg.

old between mild and strong barium stars, we find only two stars that need to be reclassified: HD 183915 (from mild to strong), and NGC 2420-173 (from strong to mild; see Table 8).

The CH and Carbon-Enhanced Metal-poor (CEMP) stars (panel e of Fig. 7, from Jorissen et al., 2016), which are the low-metallicity counterparts of barium stars, behave exactly as barium stars, in particular regarding the circular nature of most of the short-period orbits. The only notable difference is the presence of a very short-period ( $P < 10$  d) orbit, but this one is associated with a dwarf carbon star. The few CH/CEMP systems falling in the low eccentricity gap probably have inaccurate values for the eccentricity, as discussed by Jorissen et al. (2016).

The correlation between abundances and location in the  $e-P$  diagram will be discussed in Sect. 9.

## 7. Mass distribution of barium stars and their white dwarf companions

### 7.1. Methods

In previous papers, we obtained the mass (Escorza et al., 2017) and mass-ratio (Van der Swaelmen et al., 2017) distributions of barium stars. The mass distribution obtained formerly had, however, only a statistical value, since it was based on the average metallicity<sup>4</sup> of barium stars ( $[\text{Fe}/\text{H}] = -0.25$ ), rather than

<sup>4</sup> For the sake of simplicity, in the remainder of this paper, we will make no difference between metallicity (usually denoted  $Z$  in the context of stellar evolution) and  $[\text{Fe}/\text{H}]$ , thus neglecting any possible decorrelation between these two quantities due to possible enrichments of N and C in barium stars. Their due consideration would require to use grids of models accounting for specific C and N abundances, which is beyond the scope of this paper. The current STAREVOL models use the

on their individual values. Masses derived from the comparison between evolutionary tracks and location in the Hertzsprung-Russell diagram (HRD), as done by Escorza et al. (2017), are sensitive to the metallicity and therefore do require prior derivation of individual metallicities to reach the ultimate accuracy. Metallicities of barium stars have now been collected from literature, and when not available, were derived from high-resolution HERMES spectra (Raskin et al., 2011). The derivation of the atmospheric parameters was performed as described in Karinkuzhi et al. (2018), and the luminosities as described in Escorza et al. (2017). The Fe line list used is given in Table C.1, with metallicities in Table 8. Masses are then derived by matching the position of the barium star in the HRD with STAREVOL evolutionary tracks of the same metallicity (Van der Swaelmen et al., 2017; Escorza et al., 2017). In case of ambiguities, when tracks of different masses pass close to the location of the star in the HRD, we use a statistical criterion that compares the speed of evolution along the different tracks at a given location in the HRD and select the slowest one (see the discussion around Eqs. 2 and 3 in Escorza et al., 2017). The resulting metallicities and masses are listed in Table 8, along with heavy-element abundances derived as outlined by Karinkuzhi et al. (2018).

Gaia DR2 parallaxes (Gaia Collaboration et al., 2018) have been used to derive the distances and luminosities following the method outlined in Escorza et al. (2017). Gaia DR2 parallaxes result exclusively from single-star solutions. As shown by Pourbaix & Jorissen (2000), the absence of binary processing by the astrometric pipeline could lead to incorrect parallaxes only when the orbital motion with a period close to 1-yr

solar-abundance table of Asplund et al. (2009) with  $[\text{Fe}/\text{H}] = 0$  corresponding to  $Z = 0.0134$ .

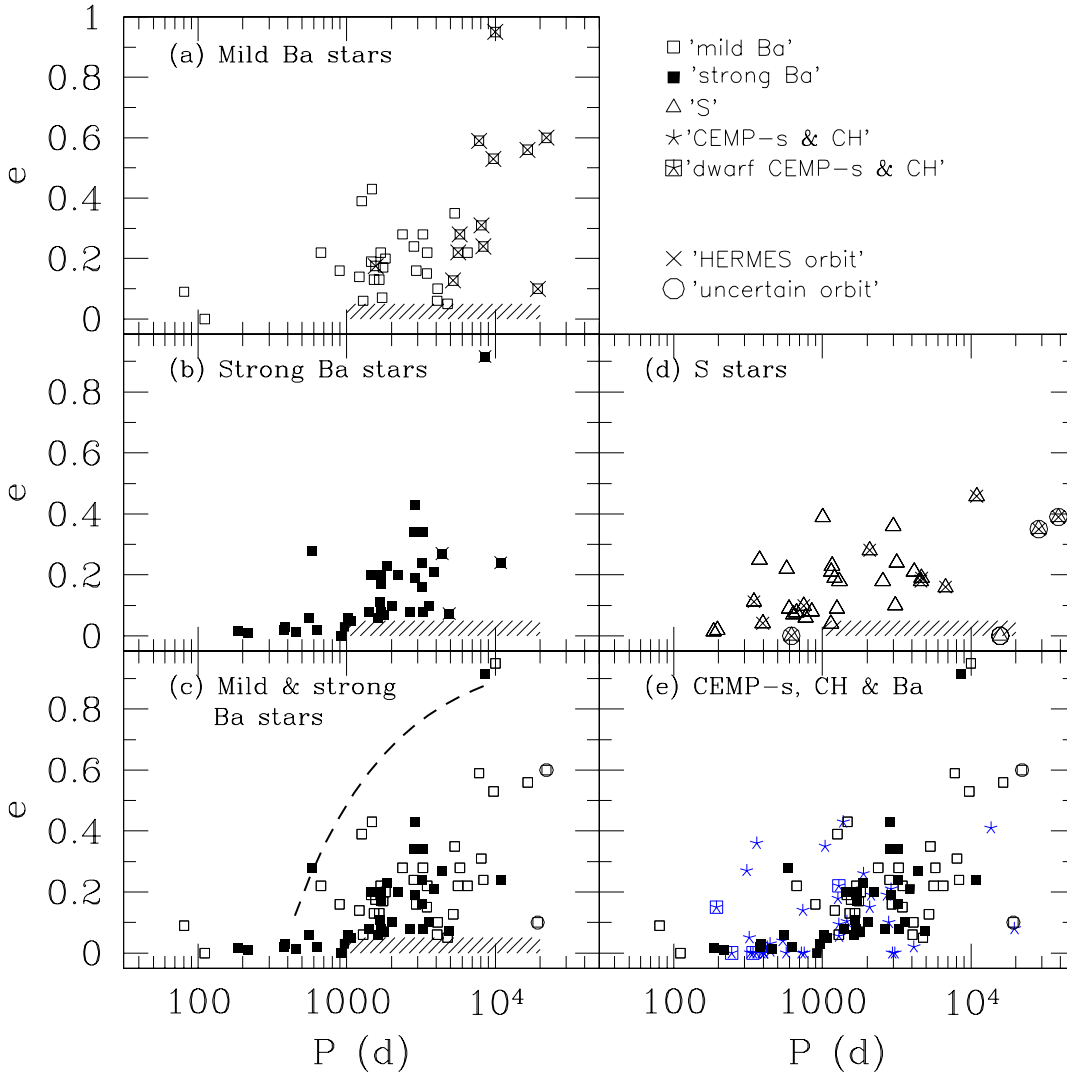


**Fig. 7.** Eccentricity – period diagrams for various samples. The meaning of the various symbols is given in the upper right panel. (a) Mild barium stars; (b) Strong barium stars; (c) Mild (open squares) and strong (filled squares) barium stars plotted together. The dashed line corresponds to the upper envelope of the data points, well represented by the condition  $143 R_{\odot} = R_{\text{Roche}} = A (1 - e) [0.38 + 0.2 \log(M_{\text{Ba}}/M_{\text{WD}})]$ , corresponding to RLOF occurring at periastron for a star of radius  $143 R_{\odot}$ .  $A$  is the semi-major axis of the orbit, linked to the orbital period  $P$  through the third Kepler law, adopting component masses of  $M_{\text{Ba}} = 2 M_{\odot}$  and  $M_{\text{WD}} = 0.65 M_{\odot}$ ; (d) S stars (triangles). The S star HD 184185, with  $P \sim 15723$  d and  $e \sim 0$ , falls in the low  $e$  – long  $P$  gap (represented by the hatched area), probably as a consequence of its still uncertain orbital parameters; (e) Same as (c), adding CEMP-s and CH stars (blue 5-branch crosses; squared crosses correspond to carbon dwarfs; from Jorissen et al., 2016). The dwarf CEMP star HE 0024-2523 with an orbital period of 3.4 d falls outside the graph boundaries.

confuses the parallactic motion. In our sample, only two stars match this criterion (DM  $-64^{\circ}4333$ , HD 24035; see Table 8), so that their masses listed in the same Table are subject to caution. Nevertheless, the corresponding WD masses for these two stars do not look peculiar.

The distribution of mass ratios<sup>5</sup> ( $q = M_{\text{WD}}/M_{\text{Ba}}$ ) is obtained from the distributions of primary masses  $M_{\text{Ba}}$  and mass-

functions  $f(M_{\text{Ba}}, M_{\text{WD}})$  under the assumption that the orbital inclination is randomly distributed according to  $g(i) = \sin i$ , since

$$f(M_{\text{Ba}}, M_{\text{WD}}) = \frac{M_{\text{WD}}^3}{(M_{\text{Ba}} + M_{\text{WD}})^2} \sin^3 i = M_{\text{Ba}} \frac{q^3}{(1 + q)^2} \sin^3 i. \quad (1)$$

To derive the distribution of  $q$ , we use the method designed by Boffin et al. (1992), which relies on a Richardson-Lucy deconvolution and has proven to be very robust and reliable (see Boffin

component of the current system), even though the demonstration that the companion is indeed a WD only comes in the present section.

<sup>5</sup> In this paper, we used the notation  $M_{\text{Ba}}$  or  $M_{\text{S}}$  to designate the barium-star or S-star mass (i.e., the primary component of the current system), and  $M_{\text{WD}}$  to designate the companion mass (i.e., the secondary



et al., 1993; Cerf & Boffin, 1994; Pourbaix, Jancart, & Boffin, 2004; Boffin, 2010, 2012; Van der Swaelmen et al., 2017).

In principle, the distribution of mass ratios  $q$  has only a statistical meaning and it is difficult to attribute a given mass ratio to a specific system. Nevertheless, this may be attempted under two different hypotheses: (i) finding the *most peaked* distribution of the companion masses, as expected if they are WD companions, or (ii) finding the distribution corresponding to a constant  $Q = M_{\text{WD}}^3/(M_{\text{Ba}} + M_{\text{WD}})^2$  value, separately for mild and strong barium stars. The two methods are discussed in turn in what follows.

Since  $M_{\text{WD}} = q \times M_{\text{Ba}}$ , the most peaked  $M_{\text{WD}}$  distribution may be obtained by performing the  $q \times M_{\text{Ba}}$  product with  $q$  and  $M_{\text{Ba}}$  sorted in opposite order (i.e., largest  $q$  combined with smallest  $M_{\text{Ba}}$ , and so on). The number of occurrence of each  $q$  in this list of products is fixed by its frequency distribution  $f(q)$  (Fig. 11) multiplied by the sample size of  $M_{\text{Ba}}$ . To limit the round-off errors due to the small sample size (only  $N = 24$  strong barium stars), the sample size has been multiplied by 10, so that each individual  $M_{\text{Ba}}$  value appears 10 times in the list, while each  $q$  bin value appears  $f(q) \times N \times 10$  times.

Of course, the above hypothesis is the most extreme one, and another attempt at finding the mass-distribution of WDs has been done under the alternative assumption of constant  $Q = M_{\text{WD}}^3/(M_{\text{Ba}} + M_{\text{WD}})^2$ . Webbink (1988) showed that the distribution of  $f(M_{\text{Ba}}, M_{\text{WD}}) \equiv Q \sin^3 i$  known at the time for barium stars was compatible with a single value of  $Q = M_{\text{Ba}} q^3/(1+q)^2$ . This correlation between the masses of the barium star and its WD companion is understandable since the more massive the barium star is, the more massive its companion had to be (and hence its WD progeny). Looking at the current sample, it appears that for the strong barium stars,  $Q$  is indeed sharply peaked at  $0.057 \pm 0.009 M_{\odot}$ , whereas for mild barium stars, the distribution of  $Q$  may be approximated by a somewhat wider Gaussian ( $0.036 \pm 0.027 M_{\odot}$ ; Fig. 8). The good agreement between observed and modelled distributions is confirmed by a Kolmogorov-Smirnov test. A similar analysis on an earlier sample of barium-star orbits (Jorissen et al., 1998) yielded similar values ( $0.049 M_{\odot}$  and  $0.035 M_{\odot}$  for strong and mild barium stars, respectively). With the result that  $Q$  is basically fixed (a very good approximation at least for strong barium stars), it will be possible to extract  $M_{\text{WD}}$  from  $Q$  and  $M_{\text{Ba}}$  for each system.

## 7.2. Results

The mass distribution is shown in Fig. 9, separately for mild and strong barium stars. Mild barium stars exhibit a clear tail towards masses up to  $5 M_{\odot}$ , whereas strong barium stars are restricted to about  $3.5 M_{\odot}$ . Fig. 10 confirms that if the threshold between mild and strong barium stars is set at 1 dex for both  $[\text{La/Fe}]$  and  $[\text{Ce/Fe}]$  (a reasonable value as revealed by Table 8), mild barium stars indeed include a tail of high-mass ( $M > 3 M_{\odot}$ ), high-metallicity ( $[\text{Fe/H}] > -0.1$ ) stars. If this high-mass tail is removed, any correlation between mass and abundances disappears.

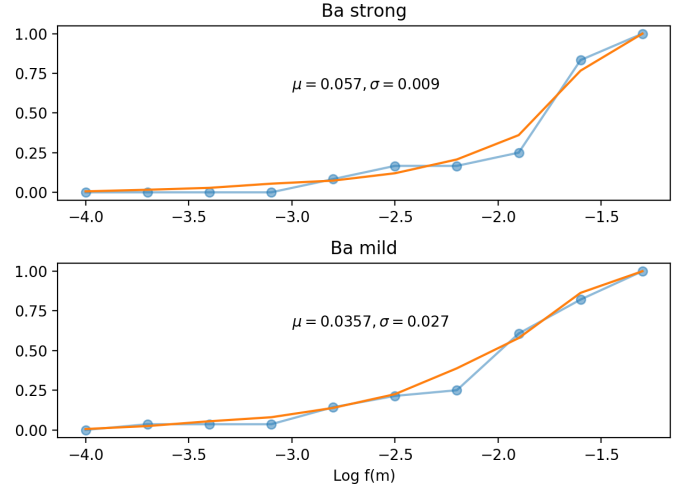


**Fig. 8.** The cumulative mass-function distributions for mild and strong barium stars, as compared to those inferred from a Gaussian distribution of  $Q = M_{\text{Ba}} q^3/(1+q)^2$  (with the Gaussian parameters as mentioned in the figure:  $\mu$  is the Gaussian average and  $\sigma$  its standard deviation, both in  $M_{\odot}$ ), convolved with random orbital inclinations.

The statistical significance of the apparent difference between the mass distributions for mild and strong barium stars may be evaluated from a Kolmogorov-Smirnov test. The maximum difference between the two cumulative frequency distributions amounts to 0.29 (bottom panel of Fig. 9). Considering that the samples comprise  $m = 30$  mild barium stars and  $n = 24$  strong barium stars, resulting in an effective sample size of  $m \times n/(m + n) = 13$ , the observed difference translates into a significance level of 79% (i.e., the first-kind error of erroneously rejecting the null hypothesis that the two distributions are similar is 21%).

The present claim that the mass distributions of mild and strong barium stars are different (albeit not to a very high significance level) is in line with similar former claims by Mennessier et al. (1997) and Jorissen et al. (1998). Although there was no such difference found in our previous paper (Fig. 14 of Escorza et al., 2017), this former contradictory result should be dismissed, because it reveals the limitations of this former analysis adopting the same metallicity for all barium stars.

The  $q (= M_{\text{WD}}/M_{\text{Ba}})$  distributions for mild and strong barium stars are shown in Fig. 11. The resulting  $M_{\text{WD}}$  distribution is shown in Fig. 12 under the most-peaked assumption, as explained in Sect. 7.1, and in Fig. 13 for the constant- $Q$  assumption.

The distributions of Fig. 12 are by construction strongly peaked (with the exception of a few non-physical “WDs” around  $0.2$  and  $0.45 M_{\odot}$  at  $0.6 - 0.7 M_{\odot}$  for WDs around mild barium stars, and at  $0.6 - 0.9 M_{\odot}$  for WDs around strong barium stars). As expected, the distributions shown in Fig. 13 for the constant- $Q$  assumption are somewhat broader than the limiting cases displayed in Fig. 12, and the small-mass outliers have disappeared. The consistency of this WD mass distribution obtained under the assumption of a constant  $Q$  is further checked by comparing in Fig. 11 the mass ratios  $q$  obtained from these WD masses and the paired barium masses (as listed in Table 8), with the  $q$  distribution obtained directly from the Lucy-Richardson inversion. Both  $q$  distributions are in good agreement, as they differ only by

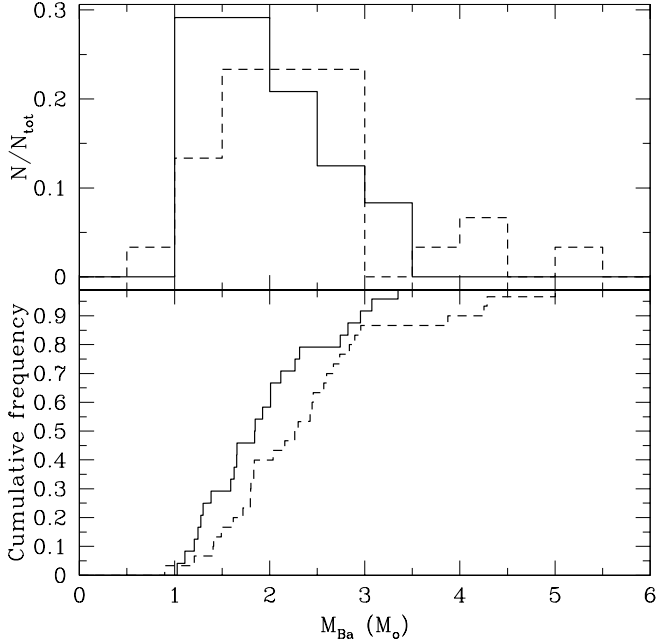


**Fig. 9.** Top panel: The mass distributions for mild (dashed lines) and strong (solid lines) barium stars. Bottom panel: The cumulative frequency distributions, to apply the Kolmogorov-Smirnov test: the maximum vertical difference between the two distributions amounts to 0.29.

the presence of sparsely populated bins in the Richardson-Lucy results (dashed lines in Fig. 11).

Another independent check of the WD masses obtained above may be performed for the few barium stars which were found to be astrometric binaries based on Hipparcos data (Pourbaix & Jorissen, 2000). A subsequent study (Jancart et al., 2005) assessed the quality of the astrometric orbital elements derived by Pourbaix & Jorissen (2000), and concluded that only HD 46407 (HIP 31205) and HD 101013 (HIP 56731) marginally satisfy the orbital quality checks (see their Table 5). Relevant data for these two systems are collected in Table 7, which reveals an agreement between the two mass values within  $2\sigma$ .

Moreover, in the case of HD 204075 ( $\zeta$  Cap), the WD companion has been detected directly from its UV radiation, using the IUE satellite (Böhm-Vitense, 1980), and the mass estimated from the observed spectrum is of the order of  $1 M_{\odot}$ , in perfect agreement with the “constant- $Q$ ” value WD mass.

For the sake of completeness, Table 8 lists as well HD 121447 although that star was not included in the luminosity determination using Gaia DR2 parallaxes. This star is suspected to be an ellipsoidal variable (Jorissen et al., 1995). The photometric analysis of the system has yielded masses of  $1.6 \pm 0.1 M_{\odot}$  and  $0.6 \pm 0.1 M_{\odot}$  for the barium star and its WD companion, respectively.

It is now possible to compare the masses of the WD companions of barium stars with field WDs. Current estimates for the average mass of the latter (represented by the red vertical dashed lines on Figs. 12 and 13) is  $0.593 \pm 0.002 M_{\odot}$  for DA WDs and  $0.676 \pm 0.014 M_{\odot}$  for DB WDs (Kleinman et al., 2013). The mass distribution of WD companions of barium stars appears to have a tail extending toward masses larger than those of field WDs. Moreover, there is a hint that WDs around strong barium stars may be more massive on average than WDs around mild

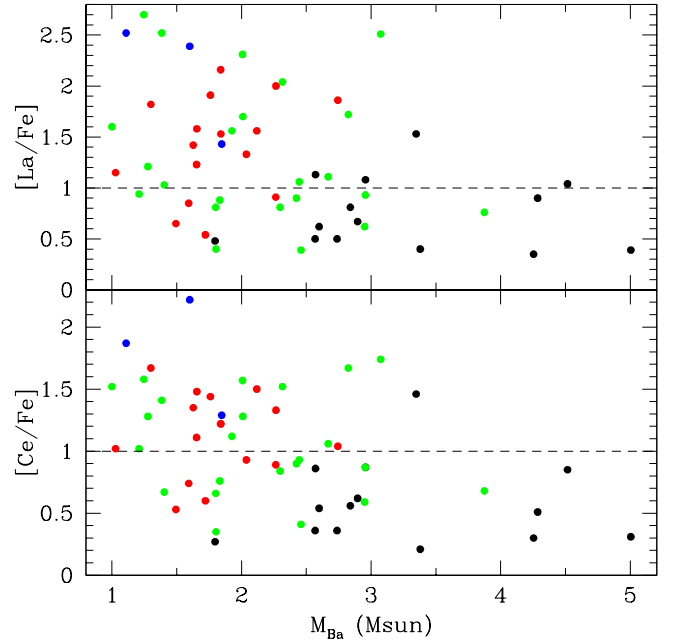


**Fig. 10.** The relationship between barium-star masses and [La/Fe] and [Ce/Fe] abundances, colour-coded according to metallicity: Blue ( $[\text{Fe}/\text{H}] \leq -0.6$ ), red ( $-0.6 < [\text{Fe}/\text{H}] \leq -0.3$ ), green ( $-0.3 < [\text{Fe}/\text{H}] \leq -0.1$ ), and black ( $-0.1 < [\text{Fe}/\text{H}]$ ).

**Table 7.** WD masses derived from the astrometrically-based  $\sin i$  (Pourbaix & Jorissen, 2000) and from the assumption of constant  $Q$ . The error bars for the WD mass derived from astrometry correspond to the error propagation from the inclination. The column labelled ‘Ba’ lists whether the star is a mild (‘m’) or strong (‘s’) barium star.

HD	HIP	Ba	$M_{\text{Ba}}$	$f(M)$	$i$	$M_{\text{WD}}$	
						(i)	(Q)
			( $M_{\odot}$ )	( $M_{\odot}$ )	( $^{\circ}$ )	( $M_{\odot}$ )	( $M_{\odot}$ )
46407	31205	s	2.12	0.035	$80 \pm 10$	$0.71^{+0.04}_{-0.02}$	0.78
101013	56731	s	1.65	0.037	$78 \pm 26$	$0.59^{+0.18}_{-0.02}$	0.68

barium stars. This trend is quite significant for the “peaked” distributions, where a Kolmogorov-Smirnov test (bottom panel of Fig. 12) yields a first-risk error of rejecting the null hypothesis of equality between the two mass distributions of only 0.44%, considering the number of stars in the sample (30 mild barium stars and 24 strong barium stars, resulting in an effective sample size of 13, as computed above) and a maximum vertical distance of 0.45 between the two cumulative frequency distributions. The difference between the average masses of WDs around mild and strong barium stars, although visible as well in the “constant- $Q$ ” WD mass distribution (Fig. 13) is however much less significant. The Kolmogorov-Smirnov test now yields a first-risk error of rejecting the null hypothesis of equality between the two distributions as large as 22% (corresponding to a maximum vertical difference of 0.18 for an effective sample size of 13, as before).



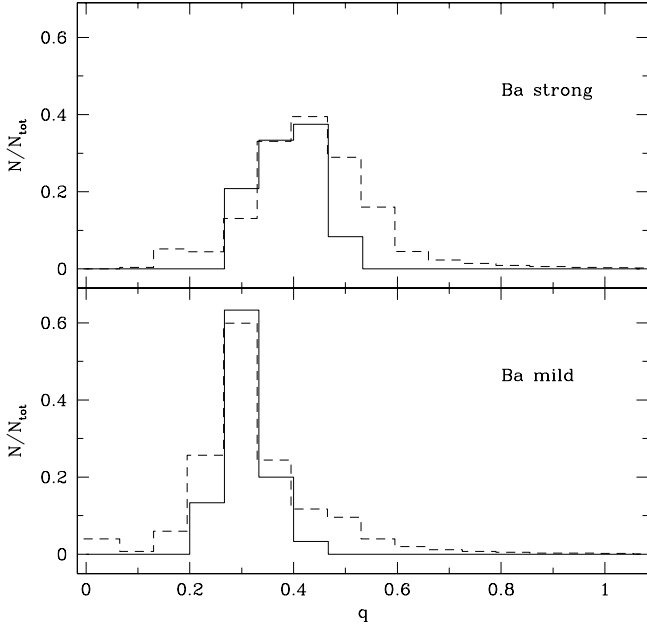


**Fig. 11.** The mass-ratio distributions for mild (bottom panel) and strong (top panel) barium stars. The dashed lines correspond to the  $q$  distribution obtained from the Richardson-Lucy inversion (see text), whereas the solid line corresponds to the  $q$  distribution rederived from the individual  $M_{\text{Ba}}$  and  $M_{\text{WD}}$  estimates (Table 8), under the assumption of a constant  $Q$  (different for mild and strong barium stars).

This difference cannot in the end be considered as very statistically significant, and as we will discuss in Sect. 9, this mitigated result may be expected from the fact that several parameters control the final level of s-process overabundance in a barium star. These parameters include the dilution factor of the accreted matter in the barium-star envelope (which depends on both its mass and the amount of accreted matter, which in turn depends on the orbital separation). They include as well the level of s-process overabundance in the accreted matter, which reflects the ability of the AGB companion to efficiently synthesize the s-process. This in turn depends on its metallicity, mass, and at a given mass, on the number of thermal pulses and third dredge-ups experienced by the AGB star (considering that the AGB evolution may have been truncated prematurely due to Roche-lobe overflow). The covariance analysis presented in Sect. 9 is a first attempt at disentangling the impact of these intricate effects on the final overabundance level.

## 8. Mass distribution of the WD progenitor and initial mass ratio of the system

In this section, we derive the mass distribution of the WD progenitor (that will be denoted  $M_{\text{AGB,ini}}$ ) and compare it with the mass of the barium star ( $M_{\text{Ba}}$ ), expecting that  $q' \equiv M_{\text{AGB,ini}}/M_{\text{Ba}} > 1$ , unless mass accretion by the barium star has substantially increased its current mass over its initial value. For the purpose of deriving  $M_{\text{AGB,ini}}$ , we use the most recent full-range initial – final mass relationship (IFMR) as derived by El-Badry et al. (2018) from the Gaia Data Release 2. The IFMR has been applied to the WD masses listed in Table 8 to get  $M_{\text{AGB,ini}}$ . The resulting mass ratio  $q'$  is shown in the bottom panel of

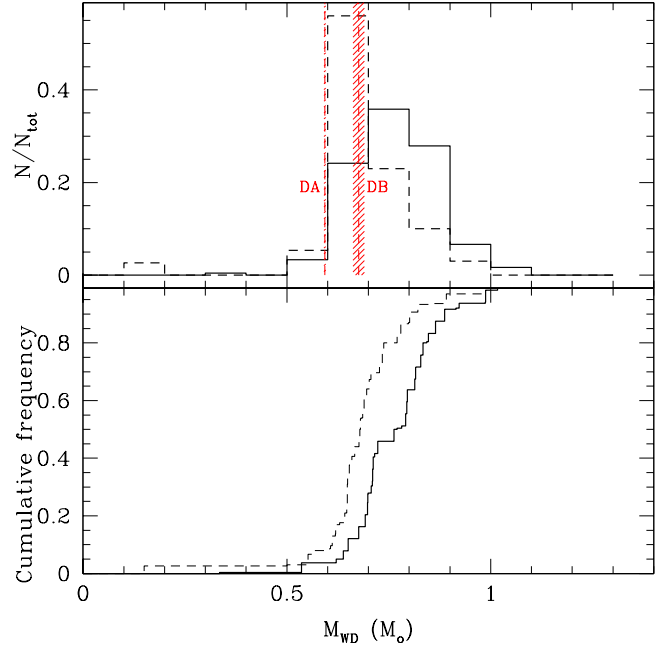


**Fig. 12.** Top panel: The white-dwarf mass distribution for mild and strong barium stars (represented by dashed and solid lines, respectively), under the hypothesis of maximum concentration. The red shaded areas labelled DA and DB correspond to the average masses ( $\pm 1\sigma$ ) for field WDs. Bottom panel: Same as top, but displayed as cumulative frequency distributions, to apply the Kolmogorov-Smirnov test. The maximum vertical distance between the two curves is 0.45.

Fig. 14. This “initial”  $q'$  distribution appears to be very different among mild and strong barium stars. As shown on the top panel of Fig. 14, this difference may ultimately be traced back to the difference between the  $Q$  values characterizing mild and strong barium stars (Fig. 8). Nevertheless, this constitutes a clear difference among mild and strong barium stars, and one may wonder whether it could be the cause for their different levels of chemical pollution. This question will be addressed in Sect. 9.

Of course, the procedure used here to derive  $M_{\text{AGB,ini}}$  assumes that the binary evolution did not affect the IFMR, and there is no guarantee thereof, quite to the contrary. Still, most of the barium systems displayed in the upper right panel of Fig. 14 have  $q' > 1$  as expected, the only exceptions being the mild barium stars with the lowest masses (open circles falling below the  $q' = 1$  line). Some of these have moreover WDs with masses lower than  $0.5 M_{\odot}$ , which is unphysical since it corresponds to progenitors which never reached the TP-AGB (see, e.g., Merle et al., 2016), and thus could not trigger the s-process whose ashes are responsible for making the barium star.

On the contrary, some of the WD companions to barium stars have large masses (with a few just above  $1 M_{\odot}$ ), pointing towards initial AGB masses larger than  $5 M_{\odot}$  (top panel of Fig. 14). It is worth noting that AGB stars of such large masses and with solar (or slightly subsolar) metallicities are not able to produce substantial s-process enrichments any longer (see, e.g., Cristallo et al., 2015; Karakas & Lugaro, 2016; Cseh et al., 2018). In that sense, these WD masses above  $1 M_{\odot}$  derived under the “constant- $Q$ ” assumption are likely somewhat overestimated (note that the “most-peaked” WD distribution in Fig. 12 is in that respect preferable, as it contains just one WD with a mass just

**Table 8.** Abundances for s-process elements in barium stars, from various sources, as listed in the column Ref. The second column, labelled Ba, lists whether the star is considered as mild (m) or strong (s) barium star. Assignment shifts (based on the abundances; see text) are indicated by an arrow. For the sake completeness, the other columns list the component masses and orbital elements. Possibly inaccurate masses for the two stars with orbital periods close to 1 yr are listed in slanted face (see text).

HD/DM	Ba	$T_{\text{eff}}$ (K)	$\log g$	$L_{\text{min}}$	$L$	$L_{\text{max}}$	$M_{\text{Ba}}$ ( $M_{\odot}$ )	$M_{\text{WD}}$ ( $M_{\odot}$ )	$P$ (d)	$e$	$f(M)$ ( $M_{\odot}$ )	[Fe/H]	[Y/Fe]	[Zr/Fe]	[La/Fe]	[Ce/Fe]	[hs/lr]	Ref
−64°4333	s	4900 ± 100	2.6	34	37	40	1.4 <sup>+0.1</sup> <sub>−0.1</sub>	0.61	386	0.03	0.068	−0.10	1.13	1.12	2.52	1.41	0.84	2
−42°2048	s	4400 ± 100	1.6	170	234	303	1.9 <sup>+0.7</sup> <sub>−0.5</sub>	0.74	3260	0.08	0.065	−0.23	0.95	0.96	1.56	1.12	0.38	2
−14°2678	m	5200 ± 100	3.1 ± 0.2	57	73	92	3.0 <sup>+0.2</sup> <sub>−0.2</sub>	0.80	3470	0.22	0.023	0.01	1.02	0.85	1.08	0.87	0.04	2
−01°3022	m	4832 ± 25	2.7 ± 0.4	51	56	61	1.6 <sup>+0.1</sup> <sub>−0.1</sub>	0.55	3253	0.28	0.016	−0.14	0.58	0.71	0.44	0.33	−0.26	4
5424	s	4728 ± 80	2.5 ± 0.0	33	60	90	1.3 <sup>+0.4</sup> <sub>−0.3</sub>	0.59	1881	0.23	0.005	−0.43	1.30	1.05	1.82	1.67	0.57	1
16458	s	4550 ± 25	1.8 ± 0.2	205	217	229	1.9 <sup>+0.1</sup> <sub>−0.1</sub>	0.72	2018	0.1	0.041	−0.64	1.06	1.29	1.43	1.29	0.19	1
18182	m	4858 ± 31	2.5 ± 0.4	60	65	71	1.8 <sup>+0.2</sup> <sub>−0.1</sub>	0.59	8059	0.31	0.0002	−0.17	0.50	0.35	0.40	0.35	−0.05	2
20394	s	4926 ± 17	2.5 ± 0.0	578	69	82	2.0 <sup>+0.2</sup> <sub>−0.2</sub>	0.76	2226	0.2	0.002	−0.27	1.00	1.14	1.70	1.28	0.42	2
24035	s	4700 ± 100	2.5 ± 0.2	13	26	39	1.3 <sup>+0.3</sup> <sub>−0.2</sub>	0.57	377.8	0.3	0.047	−0.23	1.35	1.20	2.70	1.58	0.87	2
27271	m	5022 ± 40	2.9 ± 0.5	68	82	98	2.9 <sup>+0.2</sup> <sub>−0.2</sub>	0.79	1693	0.22	0.024	−0.07	0.77	0.79	0.67	0.62	−0.13	1
31487	s	4960 ± 50	3.1 ± 0.2	124	141	160	3.4 <sup>+0.2</sup> <sub>−0.3</sub>	1.03	1066	0.05	0.038	−0.04	1.23	1.11	1.53	1.46	0.32	1
40430	m	4930 ± 29	2.4 ± 0.2	74	84	95	2.3 <sup>+0.2</sup> <sub>−0.2</sub>	0.68	5609	0.22	0.0025	−0.34	0.76	0.58	0.91	0.89	0.23	2
43389	s	4000 ± 50	2.0 ± 0.5	196	260	330	1.8 <sup>+0.4</sup> <sub>−0.3</sub>	0.72	1689	0.08	0.043	−0.35	0.91	0.32	1.53	1.22	0.76	1
44896	s	4300 ± 100	0.7	526	676	841	3.0 <sup>+1.2</sup> <sub>−1.0</sub>	0.96	629	0.02	0.048	−0.25	1.16	0.81	0.93	0.87	−0.09	11
46407	s	4854 ± 100	2.2 ± 0.4	35	83	135	2.1 <sup>+0.6</sup> <sub>−0.7</sub>	0.78	457	0.013	0.035	−0.35	1.15	1.28	1.56	1.50	0.31	1
49641	s	4400 ± 100	1.5 ± 0.2	345	457	579	2.7 <sup>+1.2</sup> <sub>−0.8</sub>	0.91	1785	0.07	0.003	−0.3	0.89	0.53	1.86	1.04	0.74	2
49841	m	5200	3.2	49	61	74	2.8 <sup>+0.2</sup> <sub>−0.2</sub>	0.78	897	0.16	0.032	0.2	0.85	0.65	0.81	0.56	−0.06	9
50082	s	4789 ± 100	2.4 ± 0.5	60	63	66	1.6 <sup>+0.3</sup> <sub>−0.2</sub>	0.67	2896	0.19	0.027	−0.32	0.86	1.04	1.42	1.35	0.44	1
51959	m	4814 ± 34	3.2 ± 0.2	11	13	16	1.2 <sup>+0.1</sup> <sub>−0.1</sub>	0.47	9718	0.53	0.0005	−0.21	0.98	1.25	0.94	1.02	−0.13	4
53199	m	5119 ± 28	2.9 ± 0.2	47	55	64	2.5 <sup>+0.1</sup> <sub>−0.1</sub>	0.71	8314	0.24	0.028	−0.20	0.68	0.70	1.06	0.93	0.31	2
58121	m	4600 ± 100	1.8 ± 0.2	121	142	163	2.6 <sup>+0.5</sup> <sub>−0.4</sub>	0.73	1214	0.14	0.015	−0.01	0.41	0.26	0.50	0.36	0.10	2
58368	m	5000 ± 100	2.6 ± 0.2	37	43	49	2.6 <sup>+0.1</sup> <sub>−0.2</sub>	0.73	672	0.22	0.021	0.04	0.85	0.60	1.13	0.86	0.27	2
59852	m	5000 ± 100	2.2 ± 0.2	81	90	100	2.5 <sup>+0.2</sup> <sub>−0.3</sub>	0.71	3464	0.15	0.0022	−0.22	0.40	0.27	0.39	0.41	0.06	2
77247	m	5050 ± 100	2.5 ± 0.5	306	346	388	3.9 <sup>+0.1</sup> <sub>−0.2</sub>	0.94	80	0.09	0.005	−0.13	0.73	0.75	0.76	0.68	−0.02	4
84678	s	4600 ± 100	1.7 ± 0.2	154	189	227	2.3 <sup>+0.6</sup> <sub>−0.5</sub>	0.83	1630	0.06	0.062	−0.13	1.09	1.21	2.04	1.52	0.63	2
88562	s	4000 ± 50	2.0 ± 0.5	240	277	321	1.0 <sup>+0.1</sup> <sub>−0.1</sub>	0.51	1445	0.2	0.048	−0.53	0.93	0.43	1.15	1.02	0.41	1
91208	m	5093 ± 67	2.9 ± 0.3	35	9	39	2.3 <sup>+0.1</sup> <sub>−0.2</sub>	0.68	1754	0.17	0.022	−0.16	0.94	0.61	0.81	0.84	0.05	2
92626	s	4800 ± 100	2.3	171	214	259	3.1 <sup>+0.4</sup> <sub>−0.6</sub>	0.98	918	0.	0.042	−0.15	0.99	1.21	2.51	1.74	1.02	2
95193	m	5008 ± 22	2.8 ± 0.1	59	69	79	2.7 <sup>+0.1</sup> <sub>−0.1</sub>	0.76	1653	0.13	0.026	−0.04	0.75	0.26	0.50	0.36	−0.07	2
98839	m	4917 ± 34	2.3 ± 0.6	276	332	395	4.3 <sup>+0.2</sup> <sub>−0.2</sub>	1.00	16471	0.56	0.056	−0.05	0.10	0.17	0.35	0.30	0.19	4
101013	s	4722 ± 32	2.3 ± 0.2	77	108	141	1.7 <sup>+0.3</sup> <sub>−0.3</sub>	0.68	1711	0.2	0.037	−0.40	1.17	0.97	1.23	1.11	0.10	4
104979	m	5100 ± 100	2.7 ± 0.2	80	95	111	2.7 <sup>+0.1</sup> <sub>−0.2</sub>	0.75	19295	0.08	-	−0.26	0.71	0.85	1.11	1.06	0.31	6
107541	s	5000 ± 100	3.2 ± 0.2	8.9	11	14	1.1 <sup>+0.2</sup> <sub>−0.1</sub>	0.54	3570	0.1	0.029	−0.63	1.53	1.35	2.52	1.87	0.75	2
119185	m	4919 ± 18	2.5 ± 0.0	65	77	90	1.7 <sup>+0.2</sup> <sub>−0.2</sub>	0.57	22065	0.6	-	−0.42	0.30	0.21	0.54	0.60	0.32	2
121447	s	4000 ± 50	1.0 ± 0.5	-	-	-	1.6 <sup>+0.1</sup> <sub>−0.1</sub>	0.6	185.7	0.015	0.025	−0.90	1.35	1.57	2.39	2.22	0.84	1

above 1  $M_{\odot}$ ). But except for those extreme cases, the WD mass distributions presented in Figs. 12 and 13 are compatible with current expectations from AGB s-process nucleosynthesis.

## 9. The period – mass – metallicity – abundance connection

In this section, we investigate the correlation between abundances, orbital periods, metallicities, and masses (barium star and WD companion). So far, the overabundances of s-process elements in barium stars were tested for possible correlation

Table 8. Continued.

HD/DM	Ba	$T_{\text{eff}}$ (K)	$\log g$	$L_{\text{min}}$	$L$	$L_{\text{max}}$	$M_{\text{Ba}}$ ( $M_{\odot}$ )	$M_{\text{WD}}$ ( $M_{\odot}$ )	$P$ (d)	$e$	$f(M)$ ( $M_{\odot}$ )	[Fe/H]	[Y/Fe]	[Zr/Fe]	[La/Fe]	[Ce/Fe]	[hs/ls]	Ref
123949	s	$4378 \pm 80$	$1.8 \pm 0.5$	59	92	128	$1.3^{+0.3}_{-0.1}$	0.58	8523	0.92	0.046	-0.23	0.91	0.88	1.21	1.28	0.35	1
134698	m	$4438 \pm 30$	$1.7 \pm 0.3$	163	192	225	$1.5^{+0.2}_{-0.2}$	0.53	10005	0.95	0.054	-0.57	0.56	0.59	0.65	0.53	0.02	2
139195	m	$5029 \pm 29$	$3.1 \pm 0.2$	38	44	514	$2.6^{+0.1}_{-0.1}$	0.74	5324	0.35	0.026	-0.07	0.72	0.79	0.62	0.54	-0.17	4
143899	m	$5144 \pm 26$	$2.9 \pm 0.3$	43	50	67	$2.4^{+0.1}_{-0.1}$	0.71	1461	0.19	0.017	-0.29	0.86	0.57	0.90	0.90	0.19	2
154430	s	$4200 \pm 100$	$1.2 \pm 0.2$	382	685	1046	$2.3^{+1.4}_{-0.7}$	0.81	1668	0.11	0.034	-0.36	0.93	0.97	2.00	1.33	0.71	2
178717	s	$3800 \pm 50$	$1.0 \pm 0.5$	156	1617	3189	$1.6^{+0.9}_{-0.7}$	0.66	2866	0.43	0.006	-0.52	0.79	0.44	0.85	0.74	0.18	1
180622	m	$4600 \pm 100$	$2.2 \pm 0.2$	59	63	68	$1.8^{+0.3}_{-0.2}$	0.59	4049	0.06	0.07	0.03	0.61	0.41	0.48	0.27	-0.13	2
183915	m→s	$4494 \pm 130$	$1.6 \pm 0.4$	153	266	386	$1.8^{+1.0}_{-0.6}$	0.60	4382	0.27	7E-05	-0.59	0.88	0.68	2.16	1.22	0.91	2
196673	m	$4914 \pm 9$	$2.5 \pm 0.3$	618	900	1206	$5.0^{+0.0}_{-0.1}$	1.10	7780	0.59	0.020	0.12	0.00	0.25	0.39	0.31	0.23	4
199939	s	$4710 \pm 9$	$2.4 \pm 0.4$	159	214	271	$2.8^{+0.4}_{-0.4}$	0.93	584.9	0.28	0.025	-0.22	1.38	1.19	1.72	1.67	0.41	1
200063	m	$4100 \pm 100$	$1.1 \pm 0.2$	206	753	1349	$2.0^{+1.3}_{-0.9}$	0.64	1735	0.07	0.058	-0.34	0.88	0.62	1.33	0.93	0.38	2
201657	s	$4700 \pm 100$	$2.2 \pm 0.2$	63	80	100	$1.8^{+0.5}_{-0.4}$	0.70	1710	0.17	0.004	-0.34	0.72	0.98	1.91	1.44	0.82	2
201824	s	$4937 \pm 52$	$2.6 \pm 0.2$	51	69	90	$1.7^{+0.4}_{-0.2}$	0.68	2837	0.34	0.04	-0.40	0.91	0.87	1.58	1.48	0.64	2
202109	m	4700	2.4	120	147	176	$3.4^{+0.2}_{-0.4}$	0.87	6489	0.22	0.023	-0.03	0.42	0.39	0.40	0.21	-0.10	9
204075	m	$5269 \pm 53$	$1.7 \pm 0.3$	418	561	741	$4.5^{+0.3}_{-0.2}$	1.03	2378	0.28	0.004	-0.09	1.37	1.37	1.04	0.85	-0.43	5
205011	m	$4803 \pm 21$	$2.5 \pm 0.1$	59	73	88	$1.8^{+0.3}_{-0.3}$	0.60	2837	0.24	0.034	-0.26	0.82	0.86	0.88	0.76	-0.02	4
210946	m	$4780 \pm 76$	$2.4 \pm 0.2$	50	74	99	$1.8^{+0.5}_{-0.4}$	0.59	1529	0.13	0.041	-0.29	0.77	0.56	0.81	0.66	0.07	2
211594	s	$4947 \pm 57$	$2.6 \pm 0.1$	49	63	77	$2.0^{+0.3}_{-0.2}$	0.76	1019	0.06	0.014	-0.29	1.20	1.18	2.31	1.57	0.75	2
218356	m	$4500 \pm 100$	1.8	543	733	976	$4.3^{+0.2}_{-1.1}$	1.00	111	0	4E-05	-0.06	0.45	0.26	0.90	0.51	0.35	7
223617	m	$4560 \pm 20$	$2.2 \pm 0.1$	61	65	70	$1.4^{+0.1}_{-0.1}$	0.51	1294	0.06	0.0064	-0.20	0.70	0.73	1.03	0.67	0.14	4
NGC																		
2420-173	s→m	$5150 \pm 100$	2.2	95	128	173	$3.0^{+0.3}_{-0.4}$	0.80	1479	0.43	0.008	-0.26	1.00	0.72	0.62	0.59	-0.26	10

References: (1) Karinkuzhi et al. (2018); (2) de Castro et al. (2016); (3) Allen & Barbuy (2006); (4) This work; (5) Merle et al. (2016); (6) Karinkuzhi & Goswami (2015); (7) Luck (2014) (8) Smith (1984); (9) Pereira et al. (2011); (10) Van der Swaelmen et al. (2017); (11) Smith (1984)

primarily with orbital periods (Jorissen & Boffin, 1992; Boffin & Začs, 1994; Bonačić Marinović & Pols, 2004; Abate et al., 2015a; Karinkuzhi et al., 2018), and to a lesser extent with metallicity (Jorissen et al., 2016; Merle et al., 2016). Our current analysis (especially Sect. 7.2) suggests to add barium-star and WD masses in the analysis as well (see also Merle et al., 2016).

Abundances for the barium stars were derived as described in Karinkuzhi et al. (2018), and are listed in Table 8. They are displayed in Fig. 15 as a function of the orbital period. Earlier studies (as listed above) claimed the presence of a general trend of decreasing s-process overabundance with increasing orbital period. In our data sample, this trend is visible only for Y. For Zr, La, and Ce, the trend – if any – is blurred by a large scatter. As shown by the color sequence on Fig. 15 (black – green – red – blue, corresponding to stars of decreasing metallicities; see the caption of Fig. 15), this scatter is partly due to metallicity, since high-metallicity stars (black points) appear mostly at the bottom of the cloud, whereas low-metallicity stars (blue points) appear mostly at its top. The role of metallicity is best revealed by Fig. 16, which displays the s-process efficiency expressed as  $[\text{hs/ls}] \equiv ([\text{La/Fe}] + [\text{Ce/Fe}]) - ([\text{Y/Fe}] + [\text{Zr/Fe}])$  as a function of metallicity. The trend seen on that plot is not surprising given that the efficiency of the s-process nucleosynthesis, when con-

trolled by the  $^{13}\text{C}(\alpha, \text{n})^{16}\text{O}$  neutron source, has been shown to increase with decreasing metallicity (e.g., Clayton, 1988; Cseh et al., 2018, and references therein).

The barium-star mass will play a role as well, since (i) barium-star mass and metallicity vary together (lower masses corresponding to lower metallicities, as expected; see Fig. 17), and (ii) larger barium-star masses imply larger envelope masses, and thus higher dilution of the accreted matter in the envelope (at least as long as the envelope is convective, notwithstanding any influence of a possible thermohaline mixing erasing the influence of the envelope mass; e.g., Husti et al., 2009).

To summarize the findings of this and the previous sections, we present in Table 9 the Pearson’s correlation-coefficient matrix of the variables discussed so far, and they reveal in a quantitative way most of the results discussed so far:

- (i)  $M_{\text{Ba}}$  and  $M_{\text{WD}}$  are the most strongly correlated variables, by construction, since  $M_{\text{WD}}$  has been derived from  $M_{\text{Ba}}$  under the assumption of constant  $Q \equiv M_{\text{WD}}^3 / (M_{\text{Ba}} + M_{\text{WD}})^2$ , separately for mild and strong barium stars;
- (ii) The strong correlation between  $e$  and  $P$  is the manifestation of the so-called ‘ $e - P$  diagram’;
- (iii)  $M_{\text{Ba}}$  and  $[\text{Fe/H}]$  are well correlated (Fig. 17);

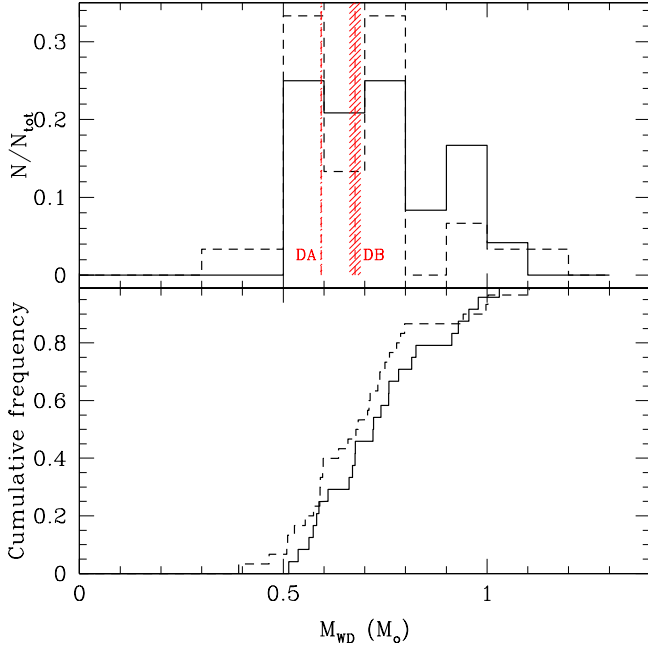


**Fig. 13.** Same as Fig. 12 derived under the assumption of constant  $Q$ . In the bottom panel, the maximum difference between the two curves is 0.18.

- (iv) S-process abundances are well correlated with each other, and moderately anti-correlated with  $P$  (the anti-correlation with  $P$  is the largest for  $[Y/Fe]$  and  $[La/Fe]$ ; Fig. 15). However, the strongest correlation between dynamical and chemical parameters is between  $q'$  and  $[La/Fe]$ ,  $[Ce/Fe]$ , as anticipated in Sect. 8.

The discussion of the implications of these results on the formation scenario of barium stars (and in particular the origin of the mild/strong nature of the barium star) is deferred to a forthcoming paper.

## 10. Conclusion

This study completed the radial-velocity monitoring of samples of mild and strong barium stars, and extrinsic S stars initiated in 1984 with the CORAVEL spectrograph. All stars monitored (37 strong barium stars, 40 mild barium stars, and 34 extrinsic S stars) turned out to be binaries, and provide a first-hand collection of 111 post-mass-transfer systems among which 105 with orbital elements will serve in the future as test bench for binary-evolution models.

Our HERMES/Mercator radial-velocity monitoring delivered the long-period orbits not yet available in the mid-course analysis published in 1998 (Jorissen et al., 1998). We found several orbits with periods in the range  $1 - 4 \times 10^4$  d ( $\sim 110$  yr). With the present study, we clearly show that the wind-accretion scenario invoked to account for the s-process pollution in the widest systems (Boffin & Jorissen, 1988; Abate et al., 2015b, 2018) is not efficient any longer in systems with periods in excess of  $4 \times 10^4$  d, due to the low accretion cross-section of the wind in such systems.

The eccentricity – period diagram further reveals that, on average, barium stars with strong s-process overabundances are restricted to the period range 200 – 5000 d (with two exceptions at

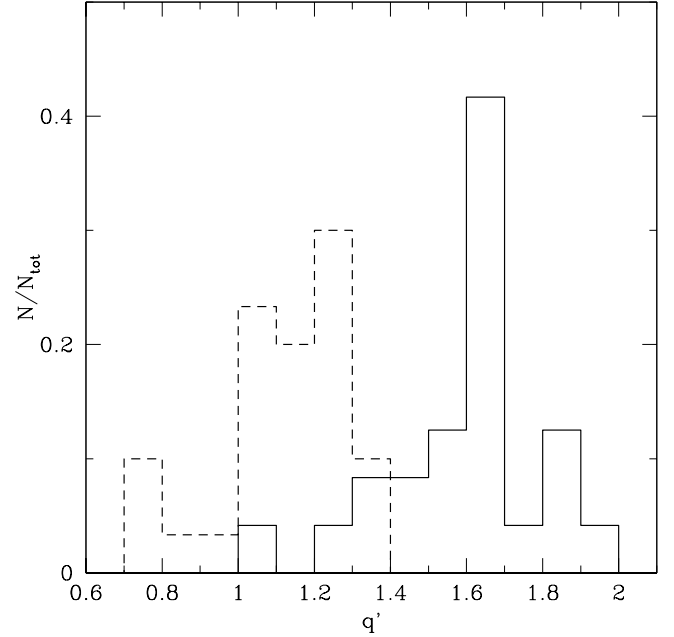
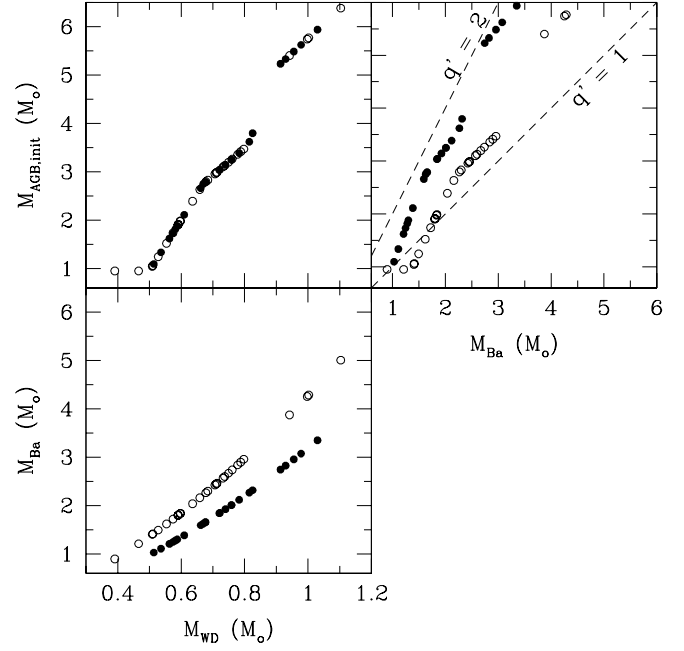


**Fig. 14.** Top panel: The relationships between the current barium-star mass ( $M_{Ba}$ ), the WD mass ( $M_{WD}$ ) and the WD-progenitor mass ( $M_{AGB,init}$ ). Mild and strong barium stars are represented by open and solid dots, respectively. Their differing sequences are caused by the adoption of two different values for  $Q = M_{WD}^3 / (M_{WD} + M_{Ba})^2$ . Bottom panel: The distribution of the “initial” mass ratio  $q' = M_{AGB,init} / M_{Ba}$ , which should in principle be larger than unity. Mild and strong barium stars are represented by dashed and solid lines, respectively.

$10^4$  d), whereas mild barium stars are found in the range 700 – 20000 d (with two exceptions at  $\sim 100$  d). The avoidance region ( $P > 10^3$  d,  $e < 0.07$ ) is confirmed, and is likely a vestige of a similar (albeit extending towards larger eccentricities) avoidance region in pre-main-sequence binaries. Almost all barium

**Table 9.** Lower-left half of the (symmetric) Pearson’s correlation-coefficient matrix of the variables  $M_{\text{Ba}}$ ,  $M_{\text{WD}}$ ,  $q'$ ,  $P$ ,  $e$ ,  $f(M_{\text{Ba}}, M_{\text{WD}})$ ,  $[\text{Fe}/\text{H}]$ ,  $[\text{Y}/\text{Fe}]$ ,  $[\text{Zr}/\text{Fe}]$ ,  $[\text{La}/\text{Fe}]$ ,  $[\text{Ce}/\text{Fe}]$ . (Non-diagonal) correlation coefficients larger than 0.4 (in absolute value) are in boldface. This value of the correlation coefficient corresponds to a two-tailed  $p$ -value of 0.17%, meaning that an uncorrelated system will produce datasets that have a Pearson correlation coefficient at least as extreme as  $\pm 0.4$  for 0.17% of the draws. For a correlation coefficient of 0.3, the two-tailed  $p$ -value raises to 2%. Strictly speaking, Pearson’s correlation requires that each dataset be normally distributed, and tests for the linearity of the correlation. The non-parametric Spearman’s rank correlation coefficients have therefore been computed as well, but do not differ meaningfully from the Pearson’s correlation coefficients listed here.

	$M_{\text{Ba}}$	$M_{\text{WD}}$	$q'$	$P$	$e$	$f(M_{\text{Ba}}, M_{\text{WD}})$	$[\text{Fe}/\text{H}]$	$[\text{Y}/\text{Fe}]$	$[\text{Zr}/\text{Fe}]$	$[\text{La}/\text{Fe}]$	$[\text{Ce}/\text{Fe}]$
$M_{\text{Ba}}$	1.										
$M_{\text{WD}}$	<b>0.913</b>	1.									
$q'$	0.165	<b>0.532</b>	1.								
$P$	-0.058	-0.174	-0.284	1.							
$e$	-0.025	-0.162	-0.304	<b>0.593</b>	1.						
$f(M_{\text{Ba}}, M_{\text{WD}})$	-0.207	-0.086	0.154	-0.126	-0.079	1.					
$[\text{Fe}/\text{H}]$	<b>0.583</b>	<b>0.471</b>	-0.078	0.001	-0.031	0.032	1.				
$[\text{Y}/\text{Fe}]$	-0.364	-0.132	0.351	<b>-0.462</b>	-0.360	0.202	-0.373	1.			
$[\text{Zr}/\text{Fe}]$	-0.285	-0.078	0.309	-0.330	-0.251	0.164	-0.331	<b>0.827</b>	1.		
$[\text{La}/\text{Fe}]$	-0.363	-0.089	<b>0.489</b>	-0.390	-0.370	0.212	<b>-0.432</b>	<b>0.718</b>	<b>0.715</b>	1.	
$[\text{Ce}/\text{Fe}]$	<b>-0.406</b>	-0.121	<b>0.498</b>	-0.357	-0.297	0.186	<b>-0.539</b>	<b>0.794</b>	<b>0.811</b>	<b>0.913</b>	1.

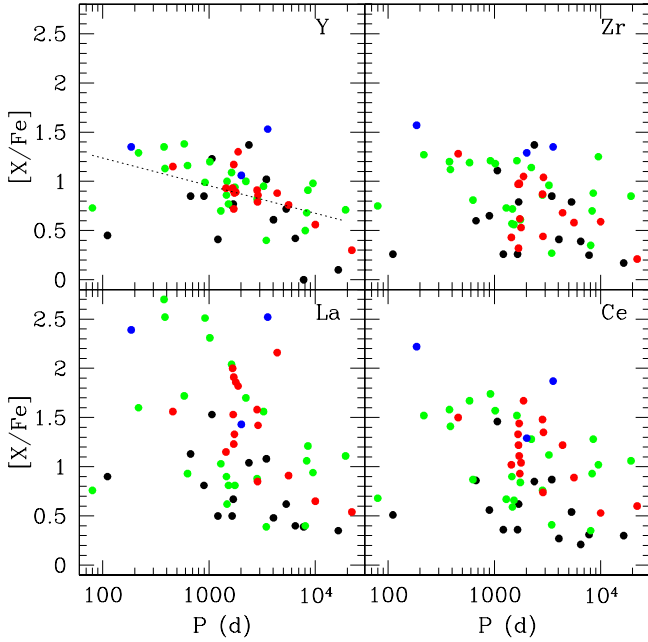


**Fig. 15.** The period – abundances relationship, for s-process elements Y, Zr, La, and Ce. In the panel corresponding to Y, the dotted line is a least-square fit to the data, illustrating the trend existing with orbital period. Blue ( $[\text{Fe}/\text{H}] < -0.6$ ), red (from  $-0.6$  to  $-0.3$ ), green (from  $-0.3$  to  $-0.1$ ), and black ( $[\text{Fe}/\text{H}] \geq -0.1$ ) symbols denote stars of increasing metallicities.

systems with periods shorter than  $10^3$  d are circular, and this property is likely attributable to the circularisation occurring as the giant star ascends the red giant branch (RGB), as demonstrated by the models of Escorza et al. (2019). Extrinsic S stars, which are still ascending the RGB, confirm this statement, since S systems with  $P < 10^3$  d are not necessarily circular, and this is the only property that they do not share with barium systems.

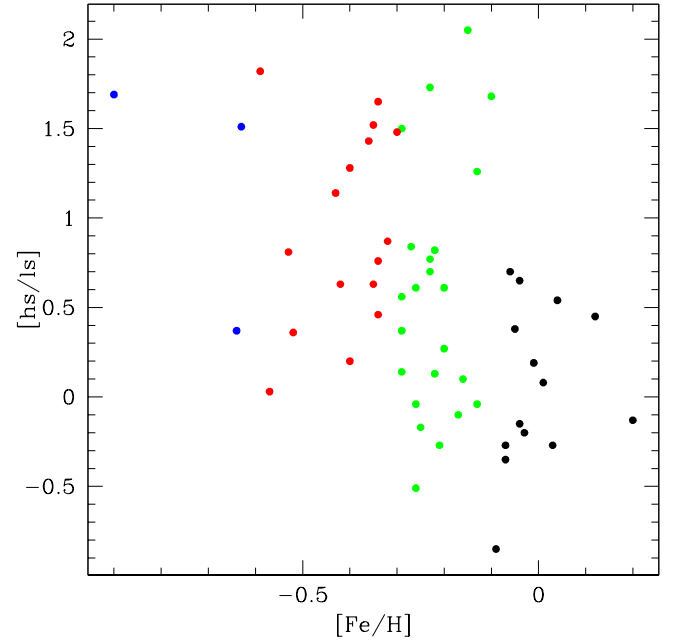


**Fig. 16.** The efficiency of the s-process, expressed as  $[\text{hs}/\text{ls}] \equiv ([\text{La}/\text{Fe}] + [\text{Ce}/\text{Fe}]) - ([\text{Y}/\text{Fe}] + [\text{Zr}/\text{Fe}])$  as a function of metallicity  $[\text{Fe}/\text{H}]$ . The colour code is as in Fig. 15.

Thanks to Gaia DR2 parallaxes and spectral-energy distribution fits, our barium-star sample could be located in the Hertzsprung-Russell diagram, and the position of individual stars compared with STAREVOL tracks of the corresponding metallicity (Siess et al., 2000; Siess & Arnould, 2008). Metallicities for the barium stars were either collected from the literature when available, or derived from Mercator/HERMES high-resolution spectra. This comparison then gives access to the barium-star masses ( $M_{\text{Ba}}$ ), which in turn yield the companion masses ( $M_{\text{WD}}$ ) under the assumption of a constant  $Q = M_{\text{WD}}^3 / (M_{\text{Ba}} + M_{\text{WD}})^2$  value (different for mild and strong bar-

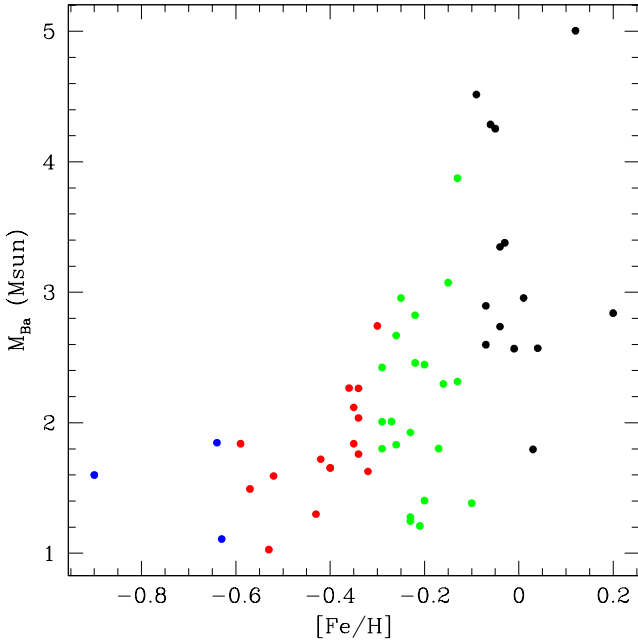


**Fig. 17.** Barium-star mass vs.  $[\text{Fe}/\text{H}]$ , colour-coded as in Fig. 15.

ium stars). This constancy was envisioned by Webbink (1988) and McClure & Woodsworth (1990), and clearly confirmed by our present extensive samples. The cause of that property, not clearly identified, deserves a specific discussion, deferred to a forthcoming paper.

The companion masses appear to be restricted in the range  $0.5 - 1.1 M_{\odot}$ , as expected for WDs. The peak of the distribution lies around  $0.55 - 0.70 M_{\odot}$ , exactly as for field DA and DB WDs. The heaviest WDs around barium stars point at AGB-progenitor masses around  $5 M_{\odot}$ , at the edge of the predictions for efficient s-process AGB nucleosynthesis.

In the hope of disentangling the various parameters involved in fixing the s-process overabundance levels in barium stars (orbital separation, dilution factor in the barium-star envelope, final AGB core mass, metallicity...), we performed a correlation analysis involving parameters  $M_1, M_2, q', P, e, f(M_1, M_2), [\text{Fe}/\text{H}], [\text{Y}/\text{Fe}], [\text{Zr}/\text{Fe}], [\text{La}/\text{Ce}]$ , and  $[\text{Ce}/\text{Fe}]$ . Significant correlations or anti-correlations (with coefficients in excess of 0.4) were found between  $P$  and  $e$ , and between s-process abundances,  $P, q'$ , and metallicity (as expected). More unexpected is the strong correlation observed between  $M_{\text{Ba}}$  and metallicity. Such a correlation must be a consequence of the age – metallicity relationship, which predicts that giants of low metallicities ( $[\text{Fe}/\text{H}] \leq -0.4$ ) in the solar neighbourhood must be older than about 5 Gyr (e.g., Fig. 3 of Feuillet et al., 2018), hence be of low mass ( $\lesssim 1.3 M_{\odot}$ ). A strong correlation is also found between  $[\text{La}/\text{Fe}]$ ,  $[\text{Ce}/\text{Fe}]$ , and the “initial” mass ratio  $q'$ . This is the strongest link found so far between dynamical and chemical abundances (it dominates over any effect related to the orbital period). It is clearly the root of the difference between mild and strong barium stars, which is visible as well in their different current  $Q$  values. It implies that strong barium stars originate from systems with a mass ratio above  $\sim 1.5$ . This is the combined result of the masses of strong barium stars being on average smaller than those of mild barium stars, and of the tendency for WDs around strong barium stars to be more massive on average. The first effect contributes to reduce the dilution factor of the accreted matter in

the barium-star envelope. This finding will certainly turn out to be a key constraint for the evolutionary models of binary stars aiming at reproducing the properties of barium stars. Initial conditions adopted in these models should certainly conform to our key finding that the “initial” mass-ratio  $q'$  is very far from being uniform, and differs for strong and mild barium stars.

**Acknowledgements.** Based on observations obtained with the HERMES spectrograph, which is supported by the Research Foundation - Flanders (FWO), Belgium, the Research Council of KU Leuven, Belgium, the Fonds National de la Recherche Scientifique (F.R.S.-FNRS), Belgium, the Royal Observatory of Belgium, the Observatoire de Genève, Switzerland and the Thüringer Landessternwarte Tautenburg, Germany. This work required a considerable observing effort, and we therefore gratefully thank all observers from the HERMES consortium and from the Instituut voor Sterrenkunde (KU Leuven) who contributed to this effort. We thank as well R. Griffin who kindly communicated his radial-velocity data of the long-period barium star 56 UMa = HD 98839. This work has made use of data from the European Space Agency (ESA) mission *Gaia* (<https://www.cosmos.esa.int/gaia>), processed by the *Gaia* Data Processing and Analysis Consortium (DPAC, <https://www.cosmos.esa.int/web/gaia/dpac/consortium>). Funding for the DPAC has been provided by national institutions, in particular the institutions participating in the *Gaia* Multilateral Agreement. This research has been funded by the Belgian Science Policy Office under contract BR/143/A2/STARLAB, and by the F.W.O. DK acknowledges the support from Science and Engineering research Board (SERB), Department of Science and technology (DST), India, through the file number PDF/2017/002338. SVE thanks Fondation ULB for its support. The Association of French Variable Star Observers (AFOEV) is acknowledged for providing the light curve of T Sgr.

## References

- Abate, C., Pols, O. R., Karakas, A. I., & Izzard, R. G. 2015, *A&A*, 576, A118
- Abate, C., Pols, O. R., Stancliffe, R. J., et al. 2015, *A&A*, 581, A62
- Abate, C., Pols, O. R., & Stancliffe, R. J. 2018, *A&A*, 620, A63
- Ake, T. B., & Johnson, H. R. 1988, *ApJ*, 327, 214
- Ake, T. B., III, & Johnson, H. R. 1992, In: Giampapa, M. S. and Bookbinder, J. A. (eds.), *Cool Stars, Stellar Systems, and the Sun*, Astronomical Society of the Pacific Conference Series Vol. 26 (San Francisco), p. 579
- Ake, T. B., Wahlgren, G. M., Johnson, H. R., & Jorissen, A. 1994, In: Caillault, J.-P. (ed.), *Cool Stars, Stellar Systems, and the Sun*, Astronomical Society of the Pacific Conference Series Vol. 64 (San Francisco), p.678
- Allen, D. M., & Barbuy, B. 2006, *A&A*, 454, 895
- Alvarez, R., Jorissen, A., Plez, B., et al. 2000, *A&A*, 362, 655
- Asplund, M., Grevesse, N., Sauval, A. J., & Scott, P. 2009, *ARA&A*, 47, 481
- Baranne, A., Mayor, M., & Poncet, J. L. 1979, *Vistas in Astronomy*, 23, 279
- Belczyński K., Mikołajewska J., Munari U., Ivison R. J., Friedjung M. 2000, *A&AS*, 146, 407
- Bidelman, W. P., & Keenan, P. C. 1951, *ApJ*, 114, 473
- Boffin, H. M. J., 2010, *A&A*, 524, A14
- Boffin, H. M. J. 2012, *Orbital Couples: Pas de Deux in the Solar System and the Milky Way*, Observatoire de Paris, 41
- Boffin, H. M. J., Cerf, N., Paulus, G. 1993, *A&A*, 271, 125
- Boffin, H. M. J., & Zacs, L. 1994, *A&A*, 291, 811
- Boffin, H. M. J., & Jorissen, A. 1988, *A&A*, 205, 155
- Boffin, H. M. J., Paulus, G., & Cerf, N. 1992, *Binaries as Tracers of Stellar Formation*, Duquenois A. & Mayor M. (eds.), Cambridge: Cambridge University Press, 26
- Boffin, H. M. J., Hillen, M., Berger, J. P., et al. 2014, *A&A*, 564, A1
- Böhm-Vitense, E. 1980, *ApJ*, 239, L79
- Bonačić Marinović, A. A., & Pols, O. R. 2004, *Mem. Soc. Astron. Italiana*, 75, 760
- Bonačić Marinović, A. A., Glebbeek, E., & Pols, O. R. 2008, *A&A*, 480, 797
- Burbidge, E. M., & Burbidge, G. R. 1957, *ApJ*, 126, 357
- Burleigh, M. R., Barstow, M. A., & Fleming, T. A. 1997, *MNRAS*, 287, 381
- Carquillat, J. M., Jorissen, A., Udry, S., & Ginestet, N. 1998, *A&AS*, 131, 49
- Carquillat, J.-M., & Prieur, J.-L. 2008, *Astronomische Nachrichten*, 329, 44
- Cerf, N., & Boffin, H. M. J. 1994, *Inverse Problems*, 10, 533
- Clayton, D. D. 1988, *MNRAS*, 234, 1
- Cristallo, S., Straniero, O., Piersanti, L., & Gobrecht, D. 2015, *ApJS*, 219, 40
- Cruzalèbes, P., Jorissen, A., Rabbia, Y., et al. 2013, *MNRAS*, 434, 437
- Cruzalèbes, P., Jorissen, A., Rabbia, Y., et al. 2014, *MNRAS*, 443, 3550
- Cruzalèbes, P., Jorissen, A., Chiavassa, A., et al. 2015, *MNRAS*, 446, 3277
- Cseh, B., Lugaro, M., D’Orazi, V., et al. 2018, *A&A*, 620, A146
- Culver, R. B., & Ianna, P. A. 1975, *ApJ*, 195, L37



- de Castro, D. B., Pereira, C. B., Roig, F., et al. 2016, *MNRAS*, 459, 4299
- Dermine, T., Izzard, R. G., Jorissen, A., & Church, R. 2011, Why Galaxies Care about AGB Stars II: Shining Examples and Common Inhabitants, 445, 447
- Dermine, T., Izzard, R. G., Jorissen, A., & Van Winckel, H. 2013, *A&A*, 551, A50
- El-Badry, K., Rix, H.-W., & Weisz, D. R. 2018, *ApJ*, 860, L17
- ESA. 1997, The Hipparcos Catalogue, ESA SP-1200
- Escorza, A., Boffin, H. M. J., Jorissen, A., et al. 2017, *A&A*, 608, A100
- Escorza, A., Karinkuzhi, D., Jorissen, A., Siess, L., Van Winckel, H., Pourbaix, D., Johnston, C., Miszalski, B., Oomen, G.-M., Abdul-Masih, M., Boffin, H.M.J., Manick, R., North, P., Shetye, S. 2019, *A&A*, submitted
- Falcon, R. E., Winget, D. E., Montgomery, M. H., & Williams, K. A. 2010, *ApJ*, 712, 585
- Frankowski A., Jorissen A. 2007, *Baltic Astronomy*, 16, 104
- Feuillet, D. K., Bovy, J., Holtzman, J., et al. 2018, *MNRAS*, 477, 2326
- Gaia Collaboration, Prusti, T., de Bruijne, J. H. J., et al. 2016, *A&A*, 595, A1
- Gaia Collaboration, Brown, A. G. A., Vallenari, A., et al. 2018, arXiv:1804.09365
- Gorlova, N., Van Winckel, H., Vos, J., et al. 2013, *EAS Publications Series*, 64, 163
- Griffin, R. F. 1984, *The Observatory*, 104, 224
- Griffin, R. F. 1991, *The Observatory*, 111, 29
- Griffin, R. F. 2006, *The Observatory*, 126, 1
- Griffin, R. F. 2008a, *The Observatory*, 128, 176
- Griffin, R. F. 2008b, *The Observatory*, 128, 474
- Griffin, R. F. 2009, *The Observatory*, 129, 6
- Griffin, R. F., & Peery, B. F. 1974, *The Observatory*, 94, 188
- Griffin, R., & Griffin, R. 1980, *MNRAS*, 193, 957
- Griffin, R. F., & Keenan, P. C. 1992, *The Observatory*, 112, 168
- Griffin, R. F., Jorissen, A., & Mayor, M. 1996, *The Observatory*, 116, 298
- Herbig, G. H. 1965, *Kleine Veröff. Remeis Sternw. Bamberg*, 4, Nr. 40, 114
- Husti, L., Gallino, R., Bisterzo, S., Straniero, O., & Cristallo, S. 2009, *PASA*, 26, 176
- Iben, I., Jr., & Tutukov, A. V. 1984, *ApJ*, 282, 615
- Izzard, R. G., Dermine, T., & Church, R. P. 2010, *A&A*, 523, A10
- Jancart, S., Jorissen, A., Babusiaux, C., & Pourbaix, D. 2005, *A&A*, 442, 365
- Johnson, H. R., Ake, T. B., & Ameen, M. M. 1993, *ApJ*, 402, 667
- Jorissen, A. 2003, *Asymptotic giant branch stars*, by Harm J. Habing and Hans Olofsson. *Astronomy and Astrophysics Library*, New York, Berlin: Springer, 2003, p. 461
- Jorissen, A., & Mayor, M. 1988, *A&A*, 198, 187
- Jorissen, A., & Mayor, M. 1992, *A&A*, 260, 115
- Jorissen, A., & Boffin, H. M. J. 1992, *Binaries as Tracers of Stellar Formation*, Duquenooy A. & Mayor M. (eds.), Cambridge: Cambridge University Press, 26, 110
- Jorissen, A., Frayer, D. T., Johnson, H. R., Mayor, M., & Smith, V. V. 1993, *A&A*, 271, 463
- Jorissen, A., Hennen, O., Mayor, M., Bruch, A., & Sterken, C. 1995, *A&A*, 301, 707
- Jorissen, A., Schmitt, J. H. M. M., Carquillat, J. M., Ginestet, N., & Bickert, K. F. 1996, *A&A*, 306, 467
- Jorissen, A., Mowlavi, N., Sterken, C., & Manfroid, J. 1997, *A&A*, 324, 578
- Jorissen, A., Van Eck, S., Mayor, M., & Udry, S. 1998, *A&A*, 332, 877
- Jorissen, A., Frankowski, A., Famaey, B., & Van Eck, S. 2009, *A&A*, 498, 489
- Jorissen, A., Van Eck, S., Van Winckel, H., et al. 2016, *A&A*, 586, A158
- Jorissen, A., Van Eck, S., & Kravchenko, K. 2016, in: Boffin, H. M. J., Hussain, G., Berger, J.-P. & Schmidtobreick, L. (eds.) *Astronomy at High Angular Resolution*, *Astrophysics and Space Science Library*, Vol. 439, Springer Verlag, Berlin, p. 137
- Käppeler, F., Gallino, R., Bisterzo, S., & Aoki, W. 2011, *Reviews of Modern Physics*, 83, 157
- Karakas, A. I., & Lugaro, M. 2016, *ApJ*, 825, 26
- Karinkuzhi, D., & Goswami, A. 2014, *MNRAS*, 440, 1095
- Karinkuzhi, D., & Goswami, A. 2015, *MNRAS*, 446, 2348
- Karinkuzhi, D., Van Eck, S., Jorissen, A., Goriely, S., Siess, L., Merle, T., Escorza, A., Van der Swaelmen, M., Boffin, H.M.J., Masseron, T., Shetye, S. & Plez, B. 2018, *A&A* 618, A32
- Keenan, P. C. 1954, *ApJ*, 120, 484
- Kjeldsen, H., & Bedding, T. R. 1995, *A&A*, 293, 87
- Kleinman, S. J., Kepler, S. O., Koester, D., et al. 2013, *ApJS*, 204, 5
- Lü, P. K., Dawson, D. W., Uggren, A. R., & Weis, E. W. 1983, *ApJS*, 52, 169
- Luck, R. E. 2014, *AJ*, 147, 137
- Lucy, L. B. 1974, *AJ*, 79, 745
- Mason, B. D., Wycoff, G. L., Hartkopf, W. I., et al. 2001, *AJ*, 122, 3466
- McClure, R. D., Fletcher, J. M., & Nemec, J. M. 1980, *ApJ*, 238, L35
- McClure, R. D. 1983, *ApJ*, 268, 264
- McClure, R. D., & Woodsworth, A. W. 1990, *ApJ*, 352, 709
- Mennessier, M. O., Luri, X., Figueras, F., et al. 1997, *A&A*, 326, 722
- Merle, T., Jorissen, A., Van Eck, S., Masseron, T., & Van Winckel, H. 2016, *A&A*, 586, A151
- Mermilliod, J.-C., Andersen, J., Latham, D. W., & Mayor, M. 2007, *A&A*, 473, 829
- Merrill P. W. 1922, *ApJ*, 56, 457
- Miller Bertolami, M. M. 2016, *A&A*, 588, A25
- Neyskens, P., van Eck, S., Jorissen, A., et al. 2015, *Nature*, 517, 174
- North, P., Berthet, S., & Lanz, T. 1994, *A&A*, 281, 775
- North, P., Jorissen, A., & Mayor, M. 2000, In: Robert F. Wing (ed.), *The Carbon Star Phenomenon*, IAU Symp. 177, Kluwer, p. 269
- Oomen, G.-M., Van Winckel, H., Pols, O., et al. 2018, *A&A*, 620, A85
- Paladini, C., Jorissen, A., Siopis, C., et al. 2014, *Proc. SPIE*, 9146, 914633
- Pereira, C. B., Sales Silva, J. V., Chavero, C., Roig, F., & Jilinski, E. 2011, *A&A*, 533, A51
- Pols, O. R., Karakas, A. I., Lattanzio, J. C., & Tout, C. A. 2003, *Symbiotic Stars Probing Stellar Evolution*, 303, 290
- Pourbaix, D., & Jorissen, A. 2000, *A&AS*, 145, 161
- Pourbaix D., Jancart S., Boffin H. M. J., 2004, *RMxAC*, 21, 265
- Raskin, G., van Winckel, H., Hensberge, H., et al. 2011, *A&A*, 526, A69
- Salaris, M., Althaus, L. G., & García-Berro, E. 2013, *A&A*, 555, A96
- Samus', N. N., Kazarovets, E. V., Durevich, O. V., et al. 2017, *Astronomy Reports*, 61, 80
- Schmid, H. M., Nussbaumer, H. 1993, *A&A*, 268, 159
- Shetye, S., Van Eck, S., Van Winckel, H., Jorissen, A., Siess, L., Goriely, S., Escorza, A., 2018, *A&A*, 620, A148
- Shetye, S., Goriely, S., Siess, L., Van Eck, S., Jorissen, A., Van Winckel, H., 2019, *A&A*, submitted
- Siess, L., Dufour, E., & Forestini, M. 2000, *A&A*, 358, 593
- Siess, L., & Arnould, M. 2008, *A&A*, 489, 395
- Smith, V. V. 1984, *A&A*, 132, 326
- Smith, V. V., & Lambert, D. L. 1988, *ApJ*, 333, 219
- Soker, N. 2000, *A&A*, 357, 557
- Stefanik, R. P., Torres, G., Latham, D. W., et al. 2011, *AJ*, 141, 144
- Stumpff, P. 1980, *A&AS*, 41, 1
- Tabur, V., Bedding, T. R., Kiss, L. L., et al. 2009, *MNRAS*, 400, 1945
- Udry, S., Jorissen, A., Mayor, M., & Van Eck, S. 1998a, *A&AS*, 131, 25
- Udry, S., Mayor, M., Van Eck, S., et al. 1998b, *A&AS*, 131, 43
- Udry, S., Mayor, M., & Queloz, D. 1999, *IAU Colloq. 170: Precise Stellar Radial Velocities*, 185, 367
- Van der Swaelmen, M., Boffin, H.M.J., Jorissen A., & Van Eck S., 2017, *A&A*, 597, A68
- Van Eck, S., Jorissen, A., Udry, S., Mayor, M., & Pernier, B. 1998, *A&A*, 329, 971
- Van Eck, S., Jorissen, A., Udry, S., et al. 2000, *A&AS*, 145, 51
- Van Eck, S., & Jorissen, A. 2002, *A&A*, 396, 599
- Van Eck, S., Neyskens, P., Jorissen, A., et al. 2017, *A&A*, 601, A10
- van Leeuwen, F. 2007, *A&A*, 474, 653
- Van Winckel, H., Lloyd Evans, T., Briquet, M., et al. 2009, *A&A*, 505, 1221
- Van Winckel, H., Jorissen, A., Gorlova, N., et al. 2010, *Mem. Soc. Astron. Italiana*, 81, 1022
- Warner, B. 1965, *MNRAS*, 129, 263
- Webbink, R. F. 1988, K.-C. Leung (ed.), *Critical Observations Versus Physical Models for Close Binary Systems*, New York, Gordon & Breach, pp. 403 - 446

## Appendix A: Spectroscopic binaries with no orbital solutions yet

This section presents velocity curves for the spectroscopic binaries with no orbital solution yet, namely the extrinsic S star BD -21°2601 (Fig. A.1), and the mild barium stars HD 50843, HD 65854, and HD 95345 (Figs. A.2, A.3, and A.4). In the figures of this section and the following, all data points posterior to JD 2454900 were obtained with the HERMES spectrograph while the previous ones are all from CORAVEL, the latter being moreover characterized by larger error bars ( $\sim 0.3 \text{ km s}^{-1}$ ).

## Appendix B: Orbital solutions

This Appendix presents all orbital solutions superimposed on the velocity data.



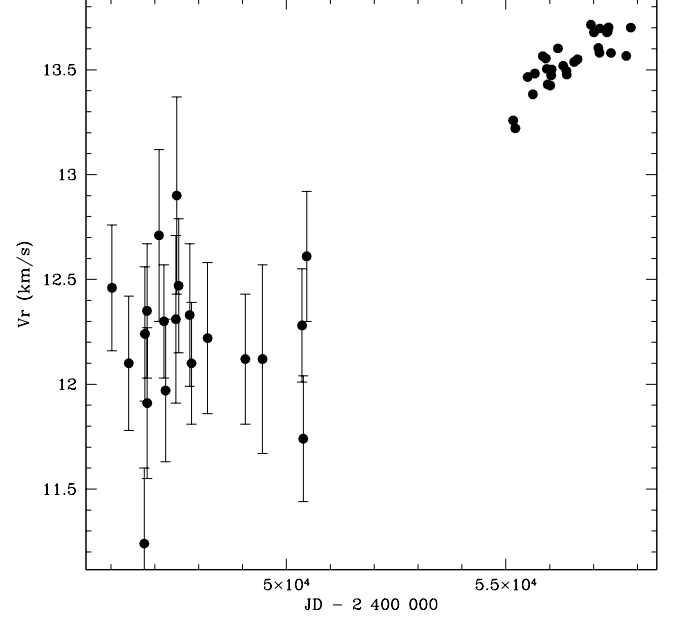
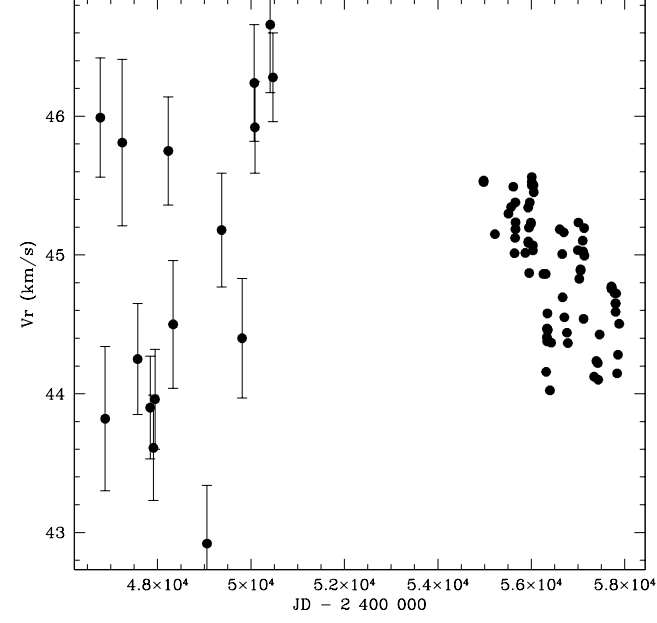


**Fig. A.2.** Same as Fig. A.1 for the mild barium star HD 50843. No offset has been applied to the CORAVEL data.

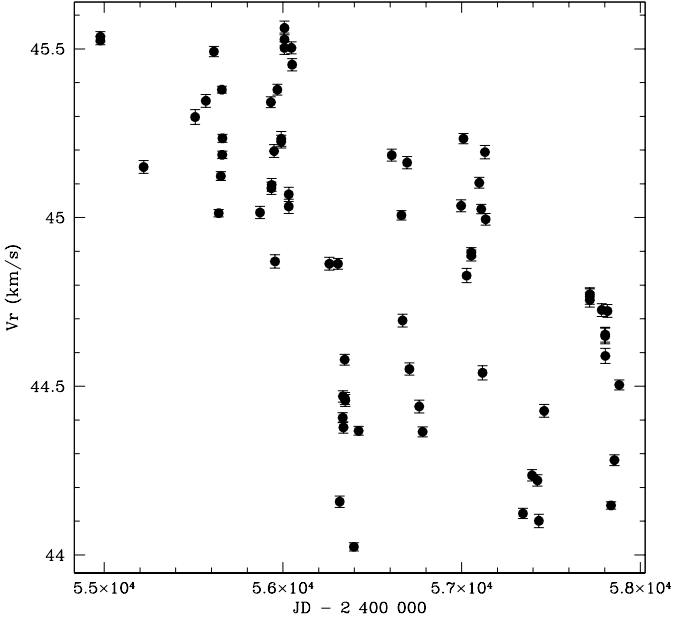


**Fig. A.1.** Top panel: Radial velocities for the S star BD -21°2601. Older data are from CORAVEL, newer from HERMES. No zero-point offset has been applied to the CORAVEL data. Bottom panel: Same as top, but for HERMES velocities only.

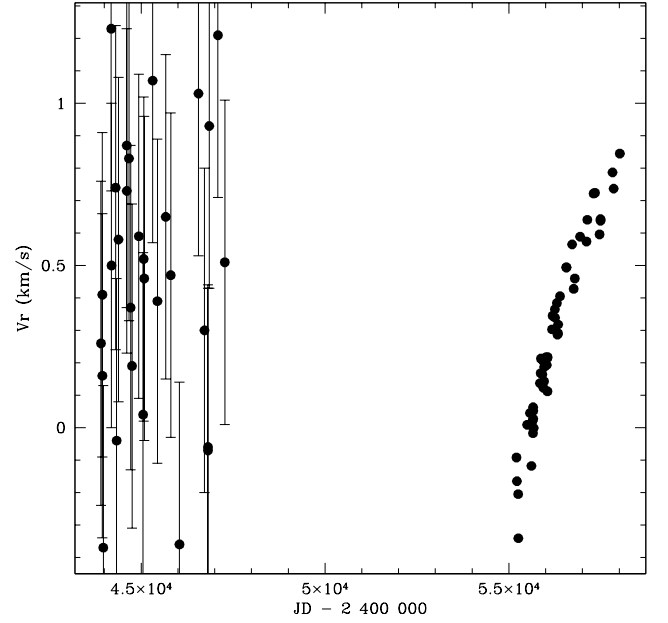


**Fig. A.3.** Same as Fig. A.1 for the mild barium star HD 65854. No zero-point offset has been applied to the CORAVEL data.

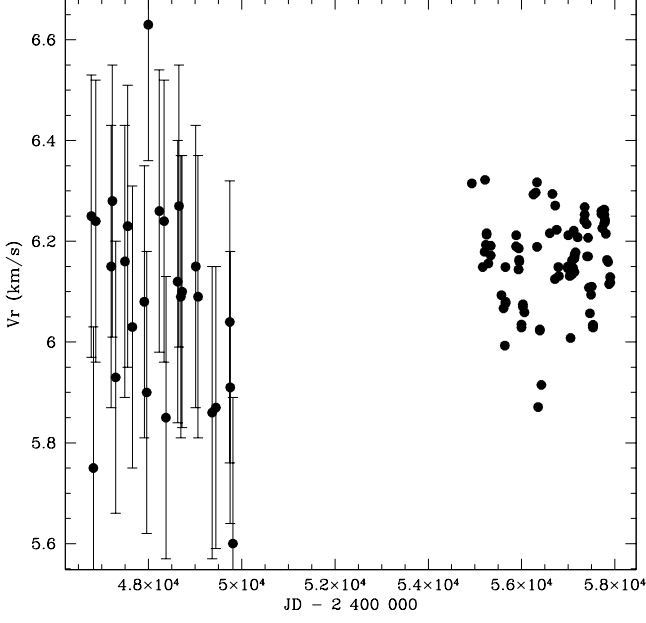


**Fig. A.4.** Top panel: Same as Fig. A.1 for the mild barium star HD 95345. A zero-point offset of  $+0.6 \text{ km s}^{-1}$  has been applied to the CORAVEL data. Bottom panel: a tentative orbit based on HERMES data only (see also Table 4).

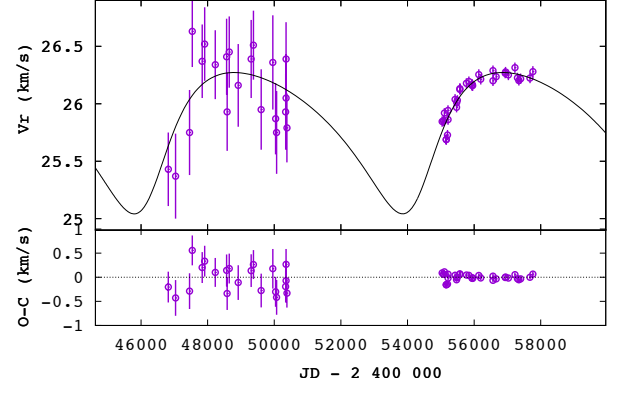


**Fig. B.1.** Upper panel: Radial velocities of the mild barium star HD 18182 and a preliminary orbit with  $P = 22 \text{ yr}$  and  $e = 0.3$ . Older data are from CORAVEL, newer from HERMES. A zero point offset of  $+0.6 \text{ km/s}$  has been applied to the CORAVEL measurements. Lower panel: O-C residuals.

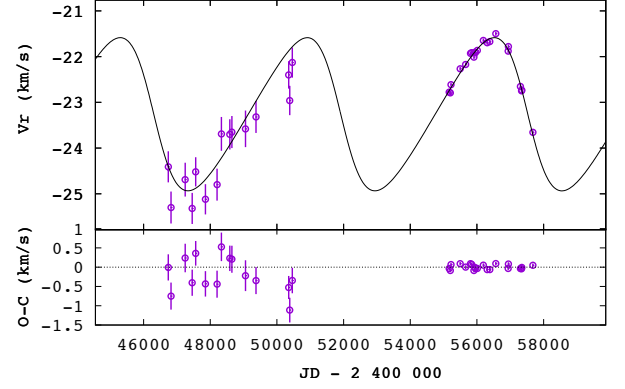
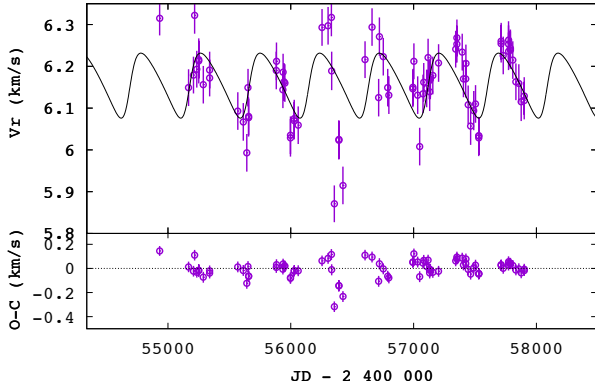


**Fig. B.2.** Upper panel: Radial velocities of the mild barium star HD 40430 and a preliminary orbit with  $P = 15 \text{ yr}$  and  $e = 0.22$ . Older data are from CORAVEL, newer from HERMES. Lower panel: O-C residuals.

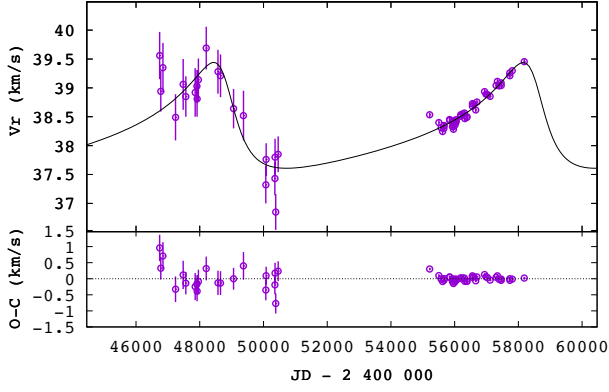


**Fig. B.3.** Upper panel: Radial velocities of the mild barium star HD 51959 and a preliminary orbit with  $P = 27$  yr and  $e = 0.53$ . Older data are from CORAVEL, newer from HERMES. Lower panel: O-C residuals.

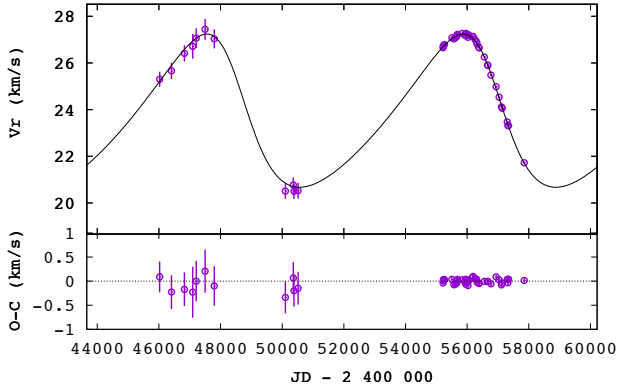


**Fig. B.4.** Upper panel: Radial velocities of the mild barium star HD 53199 and the associated orbit. Older data are from CORAVEL, newer from HERMES. An offset of +0.4 km/s has been applied to the CORAVEL data. Lower panel: O-C residuals.

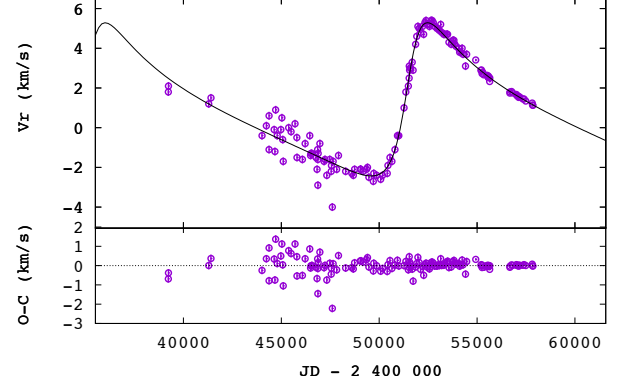


**Fig. B.5.** Upper panel: Radial velocities of the mild barium star HD 98839 (= 56 UMa) and the associated orbit. Older data are from Griffin (2008a), newer are from HERMES, according to Table 3. On this figure, the HERMES velocities are offset by +0.6 km/s to ensure consistency with Griffin's velocities. Lower panel: O-C residuals.

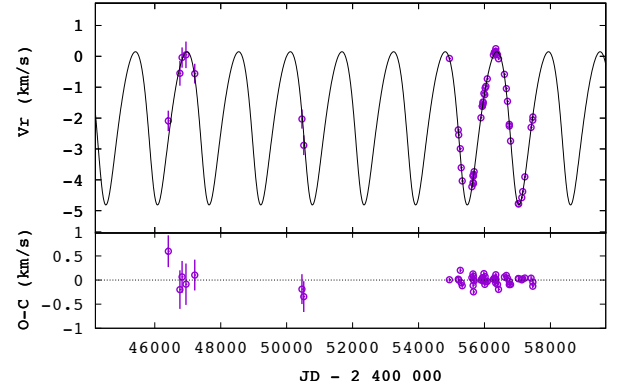


**Fig. B.6.** Upper panel: Radial velocities of the mild barium star HD 101079 and the associated orbit. Older data are from CORAVEL, newer from HERMES. An offset of +0.5 km/s has been applied to the CORAVEL data. Lower panel: O-C residuals.

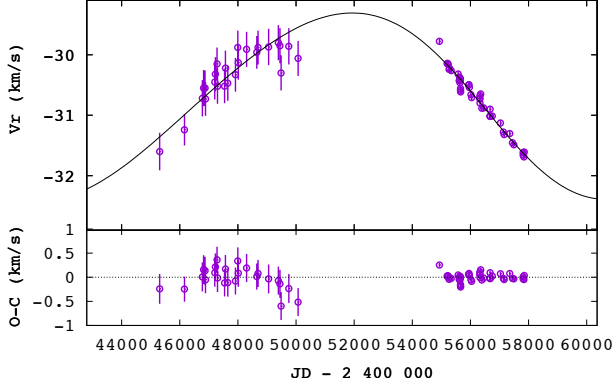


**Fig. B.7.** Same as Fig. B.1 for a preliminary orbit of HD 104979 with  $P = 53$  yr and  $e = 0.1$ . An offset of  $+0.5$  km/s has been applied to the CORAVEL data.

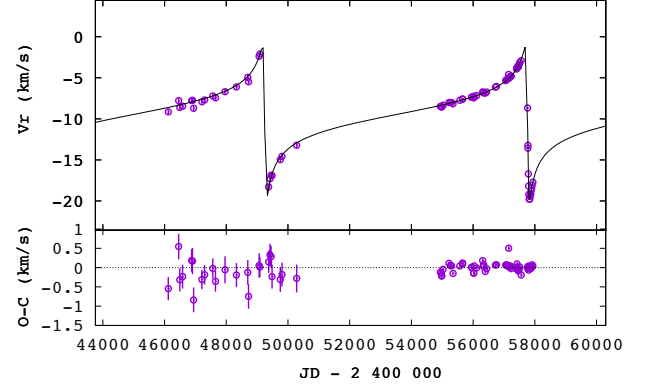


**Fig. B.9.** Upper panel: Radial velocities of the strong barium star HD 123949 and the associated orbit, having  $P = 23.3$  yr and  $e = 92$ ! Older data are from CORAVEL, newer from HERMES. An offset of  $+0.7$  km/s has been applied to the CORAVEL data. Lower panel: O-C residuals.

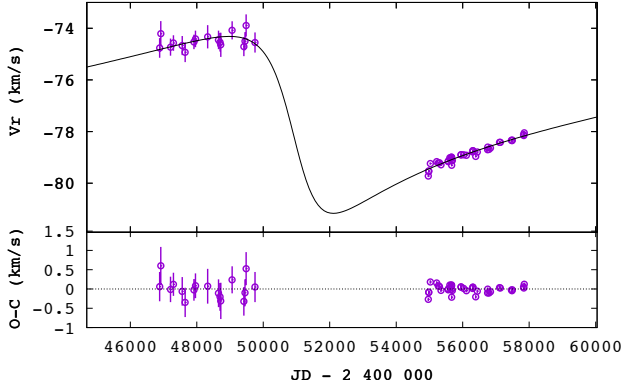


**Fig. B.8.** Upper panel: Radial velocities of the mild barium star HD 119185 and a preliminary orbit with  $P = 60$  yr and  $e = 0.6$ ! Older data are from CORAVEL, newer from HERMES. Lower panel: O-C residuals.

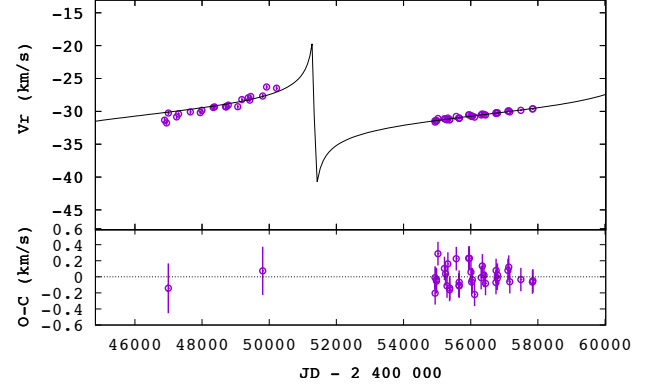


**Fig. B.10.** Upper panel: Radial velocities of the mild barium star HD 134698 and a preliminary orbit with  $P = 27$  yr and  $e = 0.95$ ! Older data are from CORAVEL, newer from HERMES. An offset of  $+0.5$  km/s has been applied to the CORAVEL data. Lower panel: O-C residuals, only shown for the data points used in the orbit derivation (see Sect. 5.4).

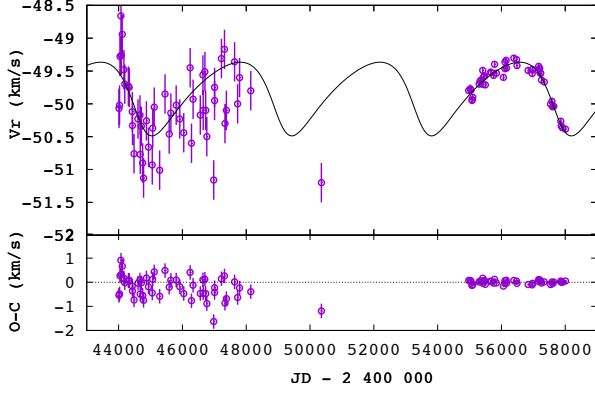


**Fig. B.11.** Upper panel: Radial velocities of the mild barium star HD 183915 and the associated orbit. Older data are from CORAVEL, newer from HERMES. Lower panel: O-C residuals.

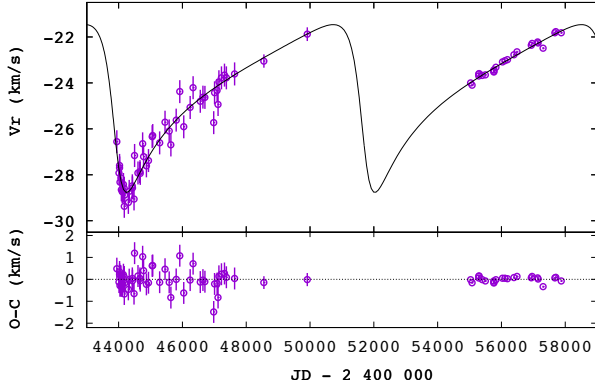


**Fig. B.12.** Upper panel: Radial velocities of the mild barium star HD 196673 and the associated orbit. Older data are from CORAVEL, newer from HERMES. Lower panel: O-C residuals.

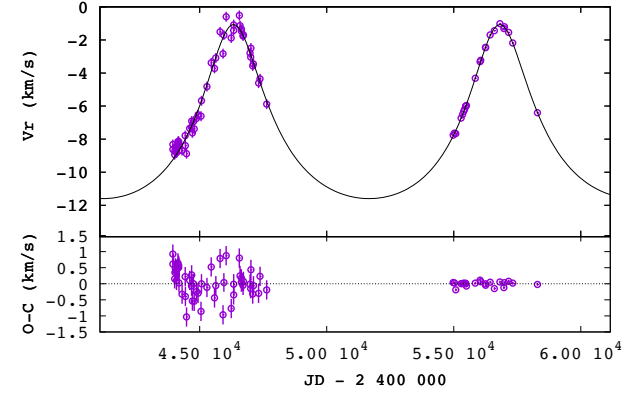
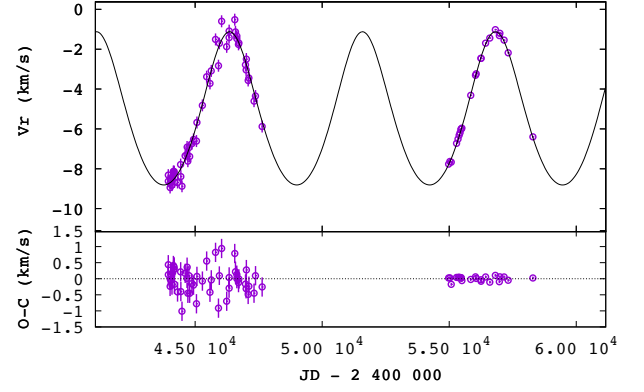


**Fig. B.13.** Two possible orbital solutions for the mild barium star HD 199394 (Top panel: the preliminary solution with  $P = 14.3$  yr and  $e = 0.11$ ; Bottom panel: another solution with  $P = 28.7$  yr, and  $e = 0.36$  is also possible, although less likely given its associated mass function of  $0.128 \pm 0.007 M_{\odot}$ , as compared to  $0.030 \pm 0.001 M_{\odot}$  for the 14 yr orbit). Older data are from CORAVEL, newer from HERMES. Lower panels: O-C residuals. An offset of  $+0.5 \text{ km s}^{-1}$  has been applied to the CORAVEL data.

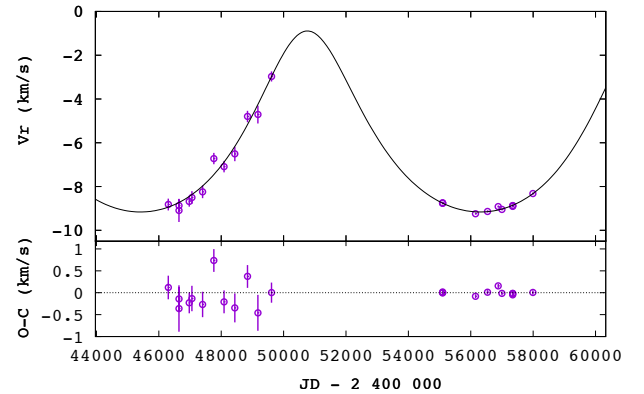


**Fig. B.14.** Upper panel: Radial velocities of the strong barium star HD 211954 and the associated orbit. Older data are from CORAVEL, newer from HERMES. Lower panel: O-C residuals.

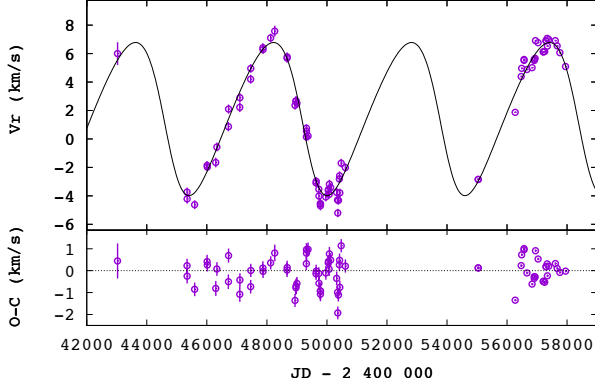


**Fig. B.15.** Upper panel: Radial velocities of the symbiotic S star HD 7351 = HR 363 and the associated orbit. Older data are from CORAVEL, newer from HERMES. Lower panel: O-C residuals.

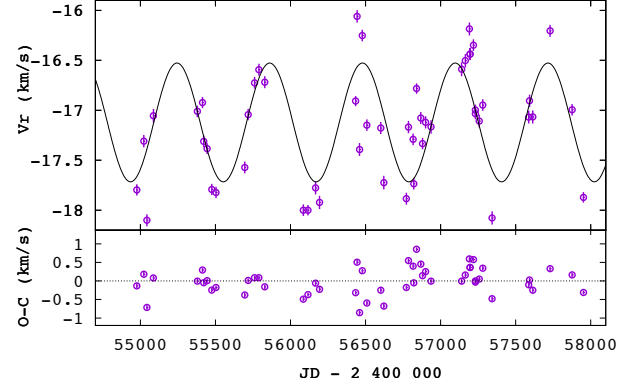


**Fig. B.18.** Upper panel: Radial velocities of the S star HD 189581 and the associated orbit. Lower panel: O-C residuals.

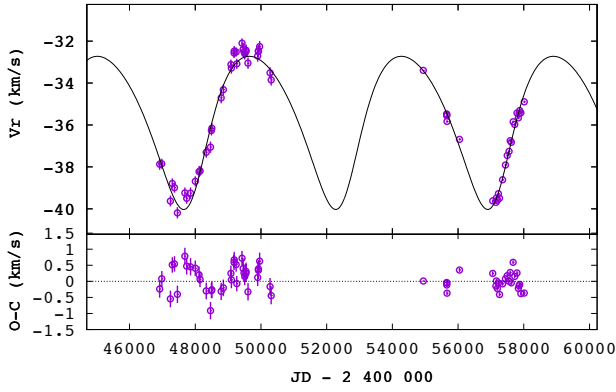


**Fig. B.16.** Upper panel: Radial velocities of the S star HD 170970 and the associated orbit. Older data are from CORAVEL, newer from HERMES. Lower panel: O-C residuals.

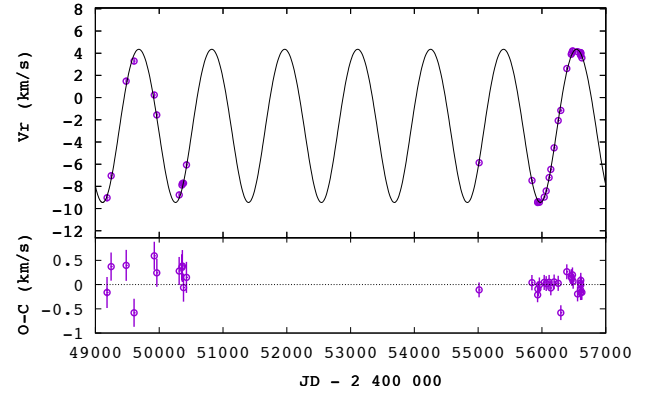


**Fig. B.19.** Upper panel: Radial velocities of the S star HD 215336 and the associated orbit. Older data are from CORAVEL, newer from HERMES. Lower panel: O-C residuals.

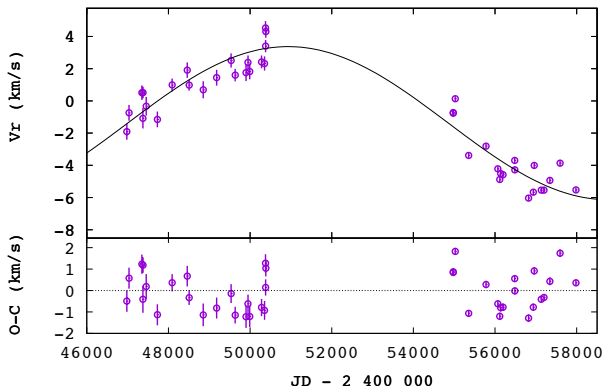


**Fig. B.17.** Upper panel: Radial velocities of the S star HD 184185 and a preliminary orbit with  $P = 43$  yr and  $e = 0$ . Older data are from CORAVEL, newer from HERMES. Lower panel: O-C residuals.

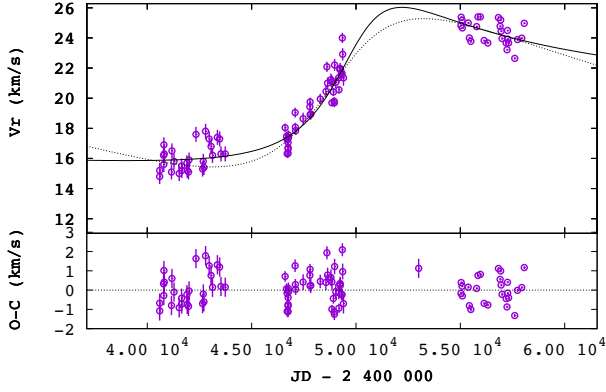


**Fig. B.20.** Upper panel: Radial velocities of the S star HD 218634 (57 Peg) and preliminary orbits with  $P = 532$  yr and  $e = 0.8$  (solid line), or  $P = 106$  yr and  $e = 0.4$  (dashed line). Older CORAVEL data are from R. Griffin (priv. comm.), newer from HERMES. Lower panel: O-C residuals.

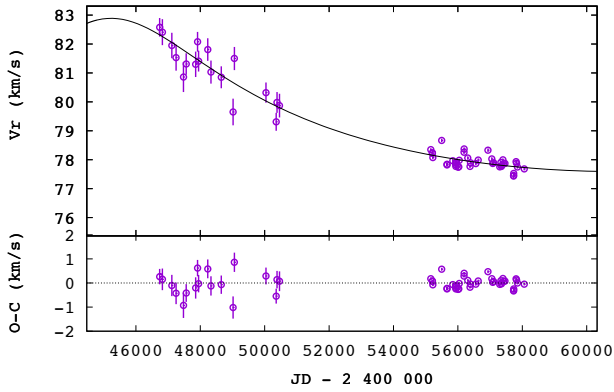


**Fig. B.21.** Upper panel: Radial velocities of the S star HDE 288833 and a preliminary orbit with  $P = 78$  yr and  $e = 0.35$ . Older data are from CORAVEL, newer from HERMES. Lower panel: O-C residuals.

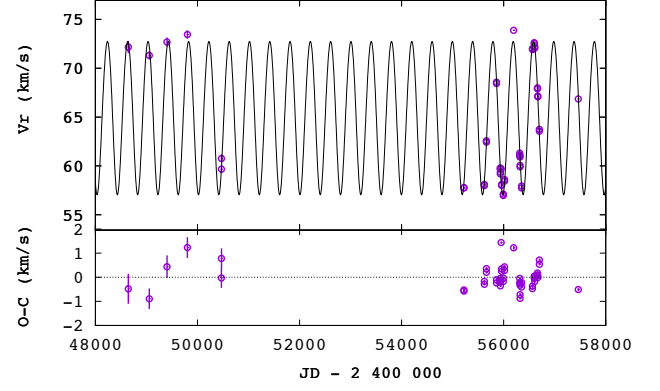


**Fig. B.22.** Upper panel: Radial velocities of the S star CD -  $28^{\circ}3719$  (= Hen 4-18) and the associated orbit. Older data are from CORAVEL, newer from HERMES. Lower panel: O-C residuals.

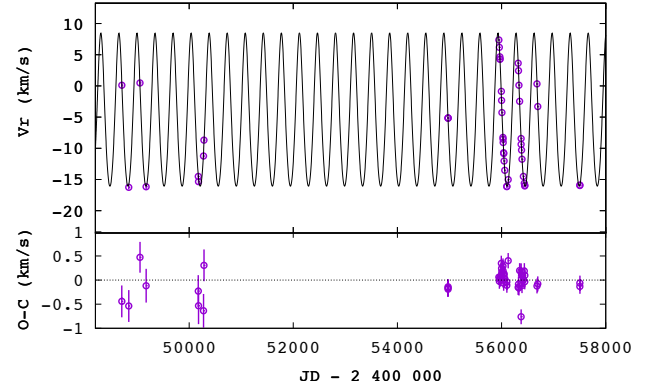


**Fig. B.23.** Upper panel: Radial velocities of the S star CD -  $25^{\circ}10393$  (= Hen 4-147) and the associated orbit. Older data are from CORAVEL, newer from HERMES. Lower panel: O-C residuals.



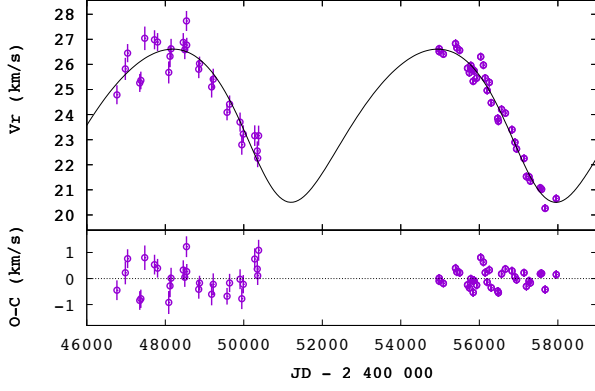


**Fig. B.24.** Upper panel: Radial velocities of the S star BD +31°4391 and the associated orbit. Older data are from CORAVEL, newer from HERMES. Lower panel: O-C residuals.

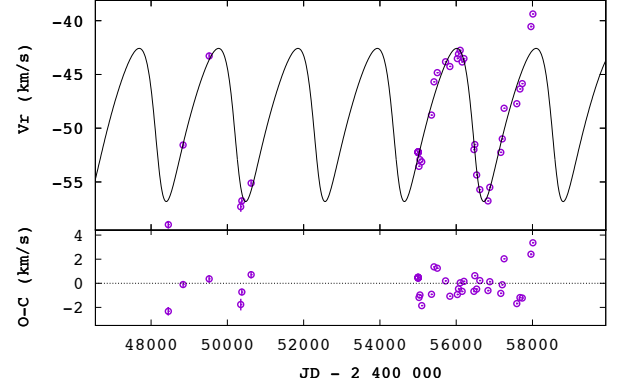


**Fig. B.27.** Upper panel: Radial velocities of the S star ER Del and the associated orbit. Older data are from CORAVEL, newer from HERMES. Lower panel: O-C residuals.

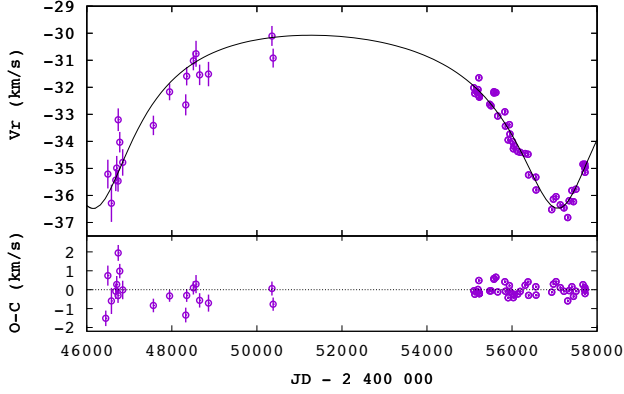


**Fig. B.25.** Upper panel: Radial velocities of the S star BD +79°156 and the associated orbit. Older data are from CORAVEL, newer from HERMES. Lower panel: O-C residuals.

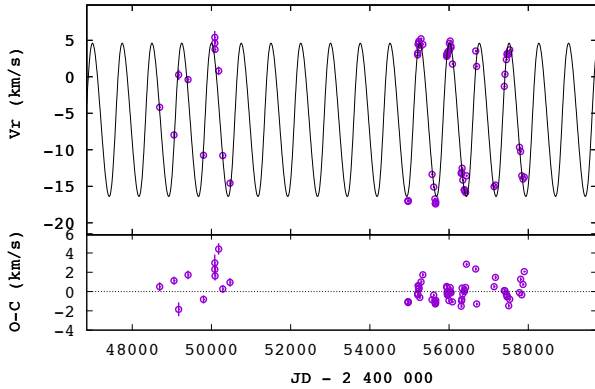


**Fig. B.26.** Upper panel: Radial velocities of the S star V420 Hya and the associated orbit. Older data are from CORAVEL, newer from HERMES. Lower panel: O-C residuals.

**Appendix C: Fe line list**

Table C.1 presents the Fe lines used to derive the metallicities of barium stars.

**Table C.1.** The Fe lines used to derive the metallicities of barium stars, along with their excitation potential and oscillator strength.

$\lambda$ (Å)	$\chi_{\text{low}}$ (eV)	$\log gf$	
5217.919	3.640	-1.719	Fe I
5223.183	3.635	-1.783	Fe I
5231.395	3.573	-2.951	Fe I
5232.940	2.940	-0.076	Fe I
5236.202	4.186	-1.497	Fe I
5243.776	4.256	-1.050	Fe I
5272.268	5.033	-1.038	Fe I
5285.127	4.434	-1.540	Fe I
5302.300	3.283	-0.720	Fe I
5321.108	4.434	-1.089	Fe I
5322.041	2.279	-2.802	Fe I
5324.179	3.211	-0.103	Fe I
5326.142	3.573	-2.071	Fe I
5339.929	3.266	-0.684	Fe I
5364.871	4.445	0.228	Fe I
5365.399	3.573	-1.020	Fe I
5379.574	3.694	-1.514	Fe I
5398.279	4.445	-0.630	Fe I
5405.775	0.990	-1.858	Fe I
5406.775	4.371	-1.620	Fe I
5410.910	4.473	0.339	Fe I
5412.784	4.434	-1.716	Fe I
5417.033	4.415	-1.580	Fe I
5434.524	1.011	-2.119	Fe I
5436.295	4.386	-1.440	Fe I
5445.042	4.386	-0.020	Fe I
5501.465	0.958	-3.046	Fe I
5506.779	0.990	-2.793	Fe I
5567.391	2.608	-2.617	Fe I
5568.810	3.635	-2.850	Fe I
5569.618	3.417	-0.486	Fe I
5572.842	3.396	-0.275	Fe I
5573.102	4.191	-1.317	Fe I
5576.089	3.430	-0.900	Fe I
5586.756	3.368	-0.120	Fe I
5587.574	4.143	-1.750	Fe I
5811.914	4.143	-2.330	Fe I
5852.219	4.548	-1.230	Fe I
5853.148	1.485	-5.180	Fe I
5853.683	4.191	-2.590	Fe I
5855.076	4.608	-1.478	Fe I
5856.088	4.294	-1.327	Fe I
5857.802	5.033	-1.767	Fe I
5858.778	4.220	-2.160	Fe I
5859.586	4.549	-0.419	Fe I
5927.789	4.652	-0.990	Fe I
5929.677	4.548	-1.310	Fe I
5930.180	4.652	-0.230	Fe I
5934.655	3.928	-1.070	Fe I
5958.333	2.176	-4.160	Fe I
5425.257	3.199	-3.220	Fe II
5432.967	3.267	-3.527	Fe II
5534.847	3.245	-2.865	Fe II
5991.376	3.153	-3.647	Fe II
6238.392	3.889	-2.600	Fe II
6247.557	3.892	-2.435	Fe II
6416.919	3.892	-2.877	Fe II
6432.680	2.891	-3.570	Fe II
6456.383	3.903	-2.185	Fe II